Scale-Resolving Simulations of a Civil Aircraft Wing Transonic Shock Buffet Experiment

Luke Masini* and Sebastian Timme†
University of Liverpool, Liverpool, L69 3GH, United Kingdom

Andrew J. Peace‡
Aircraft Research Association Ltd., Bedford, MK41 7PF, United Kingdom

The flow physics governing the shock-buffet phenomenon on swept wings remain disputed without an unequivocal description. Herein we contribute to the ongoing discussion by addressing the inherent dynamics near the onset of unsteadiness, complementing experimental data of a large aircraft wing geometry with scale-resolving simulation. **Specifically, delayed detached-eddy simulations are performed to reproduce the experiments with Reynolds number 3.75×10^6 and Mach number 0.801 and analysed using modal methods. Motivated by the recognised difficulty in simulating separating and reattaching shallow shear layers employing such techniques, we scrutinise the impact of two subgrid length-scale definitions. The simulations, using both the standard definition of maximum local spacing and a more recent vorticity-sensitive variant, are validated against experimental data from conventional steady and unsteady instrumentation and dynamic pressure-sensitive paint. We find remarkable agreement between experiment and simulation when using the vorticity-sensitive definition, whereby dominant modal features extracted from surface pressures show striking similarity in describing localised pockets of shear-layer pulsation synchronised with an outboard-propagating shock oscillation. Identified modes from simulation cover broadband content centred at a Strouhal number of approximately 0.27 which is within the experimental frequency range characteristic for swept-wing shock buffet. Modes capturing an inboard-running lower-frequency shock unsteadiness centred at a Strouhal number of approximately 0.07 are exclusive to wind-tunnel conditions. Nevertheless, modal analysis succeeds in extracting key characteristics from such practical unsteady-flow datasets. We anticipate our findings to help clarify these edge-of-the-envelope flow phenomena and to ultimately inform shock-buffet delay and control strategies.**

---

*PhD Student, School of Engineering, l.masini@liverpool.ac.uk, AIAA Student Member.

†Senior Lecturer, School of Engineering, sebastian.timme@liverpool.ac.uk, AIAA Member.

‡Chief Scientist, apeace@ara.co.uk, AIAA Senior Member.

Nomenclature

C_L =   lift coefficient

c_p =   pressure coefficient

f =   frequency, Hz

f_s =   sampling frequency, Hz

i =   snapshot index

m =   number of snapshots

n =   number of computational mesh points

p =   static pressure, Pa

Re_{MAC} =   Reynolds number based on mean aerodynamic chord (MAC)

St =   Strouhal number based on mean aerodynamic chord

t =   physical time, s

u =   streamwise velocity, m/s

Y =   spanwise coordinate, m

y^+ =   wall-normal mesh spacing in wall units

α =   angle of attack, deg.

Δ_0 =   mesh target spacing, m

Δ =   subgrid length scale

Δ_{max} =   maximum-edge subgrid length scale

$\tilde{\Delta}_\omega$ =   vorticity-sensitive subgrid length scale

η =   nondimensional spanwise position

$\Lambda_{1/4}$ =   quarter-chord sweep angle, deg.

σ =   standard deviation

μ_t/μ =   ratio of turbulent viscosity μ_t to dynamic viscosity μ

I. Introduction

TRANSONIC shock buffet on large aircraft wings remains a key challenge for aerodynamicists, with no unequivocal explanation to the flow mechanism governing its onset, despite over half a century of research [1]. At critical combinations of Mach number and angle of attack, shock-wave/boundary-layer interaction (SWBLI) on the wing surface induces self-sustained shock oscillation combined with intermittent boundary-layer separation. This aerodynamic unsteadiness, typically termed as *shock buffet*, generates unsteady loads and a consequent dynamic structural response, referred to as *buffeting*, mutually interacting with the flow. In effect, passenger comfort and safety, aircraft performance,

handling qualities, and structural fatigue life are all degraded. Moreover, certification requirements stipulate a cruise design point free from any structural vibration and buffeting, such that shock-buffet onset may limit the flight envelope at high Mach number and load factor, depending on the aircraft (specifically wing) design philosophy, motivating continuous scrutiny both from industry and academia. Notwithstanding, extensive previous research surrounding this topic has elucidated distinct characteristics on two-dimensional aerofoils and swept three-dimensional wings.

In the case of two-dimensional aerofoils, periodic shock oscillations have been identified in several experimental [2–4] and numerical studies [5–9]. The unsteadiness is characterised by narrow-band spectral peaks at low frequencies—at least two orders of magnitude lower than those associated with turbulence in the incoming boundary layer. Large shock excursions of around 20% chord length have been reported at Strouhal numbers (based on chord length and reference freestream velocity) between 0.05 and 0.08 [10]. A first model to describe these self-sustained shock oscillations is attributed to Lee [11]. Broadly, it relies on an acoustic coupling between the trailing edge and the shock wave. The hypotheses of an oscillating shock being affected by acoustic forcing and the shock directly influencing the conditions at the trailing edge have been confirmed experimentally [4, 12]. However, efforts to directly measure or simulate the exact propagation path of upstream and downstream travelling waves have led to contradictory results leaving room for debate [3, 13]. A more recent explanation of aerofoil shock buffet by Crouch *et al.* [14], and further supported by Sartor *et al.* [15], regards the phenomenon as a Hopf bifurcation with a globally unstable fluid mode appearing beyond critical conditions. Albeit the lack of one consolidated theory, the notion of an acoustic feedback loop is generally accepted. Several numerical techniques have been employed to simulate two-dimensional shock buffet, including unsteady Reynolds-averaged Navier–Stokes (RANS) simulations [5, 7, 8], detached-eddy simulations (DES), including the zonal [6] and the delayed (DDES) approach [9], and large-eddy simulations (LES) [16, 17]. Most of these studies assume a fully turbulent boundary layer upstream of the SWBLI. However, recent work on laminar profiles, where laminar-to-turbulent transition takes place in the region of the SWBLI, has reported shock excursions confined to the shock foot over smaller chordwise distances and at frequencies of over an order of magnitude higher than the fully turbulent case [18, 19]. Furthermore, complex interactions between the shock wave, pressure waves and the boundary layer have been studied using direct numerical simulation at moderate Reynolds number [20].

The exact flow physics governing finite swept-wing shock buffet is less clear, not least because of historically more limited research specifically on transport-type wings and the far more complex three-dimensional interactions involved. The reader is referred to the work by Giannelis *et al.* [21] which extensively reviews recent activities in this field. It is generally agreed that wing buffet differs from the two-dimensional case in two main aspects. First, a narrow frequency peak no longer characterises the phenomenon. Instead, swept-wing shock buffet has a broadband higher-frequency signature at Strouhal numbers between 0.2 and 0.6, based on mean aerodynamic chord (MAC) and depending e.g. on sweep angle. Second, shock oscillation takes place over shorter chordwise distances which can vary along the span depending on the extent of the separation region downstream of the shock. These particular characteristics which

suggest distinct physical mechanisms governing aerofoils/straight wings and swept wings were observed from early flight test data [22] and wind-tunnel tests [23–25]. More recent experimental tests [26–28] employing highly-instrumented wind-tunnel models have confirmed the broadband signature and have further elucidated the phenomenon by computing significant phase speeds. The advent of novel optical techniques such as dynamic pressure-sensitive paint (DPSP), essentially a fast-response pressure-sensitive paint coupled with high-frame-rate image capturing, has greatly progressed the understanding of the complex shock motion that takes place at edge-of-the-envelope conditions. Although early applications in transonic wind tunnels [29, 30] had limited resolution or coverage, more recent experiments [28, 31] have acquired unsteady pressure over the entire wing surface enabling detailed analysis of the shock dynamics.

Numerical studies undoubtedly complement this improved understanding. Notably, a systematic study employing time-marching unsteady RANS simulations [32] revealed contrasting characteristics between straight/low-sweep-angle wings and those with sweep angles above $20°$, typical for modern wing designs. At low sweep angles, shock oscillation is chordwise dominated and similar to that on aerofoils. On moderately and highly swept wings, a spanwise propagation of pressure along the shock and pockets of shock-induced separation, coined therein as buffet cells, were observed moving outboard. A related numerical study on infinite swept wings has shown similar characteristics for buffet cells, linked with transonic shock buffet, and low-speed stall cells [33]. Moreover, studies employing stability analysis on such infinite wings have identified, besides the typical aerofoil mode, monotone stationary spanwise-periodic modes on straight wings, which, with the introduction of sweep, become oscillatory with outboard propagation [34–36]. Increasingly sophisticated simulations, including scale-resolving DES [37–39], have been conducted on several geometries demonstrating the capability of capturing complex shock motion and characteristic spanwise propagation of buffet cells. Even though the time scales of shock buffet are much longer than those related to wall-bounded turbulence, hence justifying unsteady RANS simulations, scale-resolving simulations have explained the phenomenon in more detail and with a broader spectral content. The flow conditions simulated in those finite-wing studies are well-beyond the point when flow unsteadiness is first observed and do not necessarily describe the flow physics in the vicinity of onset. In this spirit, the involvement of a global instability in the onset dynamics has recently been studied on a finite wing [40]. Therein, buffet cells are linked to an unstable eigenmode while the emergence of a group of modes with reduced decay rate agrees with the aforementioned broadband frequency trend.

In this paper, we further address the inherent dynamics governing swept-wing shock-buffet onset. We aim to fill the gap in the literature surrounding transonic wing shock buffet by presenting a synergistic study combining high-quality experimental data first discussed in [28], and also analysed in [41, 42], with scale-resolving DES. Comprehensive analysis of the experimental dataset [42] has identified two distinct phenomena in shock-buffet conditions—a low-frequency shock unsteadiness for Strouhal numbers between 0.05 and 0.15 along the whole span, predominantly propagating pressure inboard, and a broadband higher-frequency behaviour for Strouhal numbers between 0.2 and 0.5, confined to the wing-tip region propagating pressure outboard towards the tip. This outboard behaviour was captured by unsteady RANS

4

simulation [43] and DDES [39] and is similar to previously reported buffet cells, believed to constitute the shock-buffet instability on conventional swept wings. However, DES is known to struggle with separated shear layers, particularly those encountered herein for incipient shock buffet, in that the transition from modelled to resolved turbulence is delayed on typical cost-aware anisotropic meshes [44]. Hence, besides the classical subgrid length scale of using a mesh cell's maximum edge length, we scrutinise the impact of a newer variant incorporating the solution-dependent vorticity vector to detect the initial, nearly two-dimensional shear layer and unlock resolved content. Resulting massive DDES datasets are analysed with data-based modal identification techniques, which are becoming routinely used in the extraction and characterisation of pertinent flow features [45, 46], and contrasted with the previous insight from experimental DPSP [42]. This work contributes to the ongoing discussion on, and renewed interest in, edge-of-the-envelope flow physics, ultimately informing future wing design and routes to buffet control.

Section II presents the test case, including the wing geometry and flow conditions, an overview of the wind-tunnel test campaign, and the computational mesh. The numerical approach using the DLR-TAU solver and an overview of the post-processing techniques are outlined in Sec. III. Results from steady-state and time-marching simulations are analysed and compared with experimental data using conventional techniques (e.g. pressure distributions and Fourier analysis) in Sec. IV, giving confidence in the numerical approach. Further comparisons between the time-accurate simulations and DPSP measurements are performed using modal analysis (proper orthogonal and dynamic mode decomposition) in Sec. V, clarifying the inherent dynamics of shock-buffet onset and the limitations of such simulations.

II. Test Case

A. Geometry and Flow Conditions

The test case is a half wing-body configuration called RBC12 which represents a commercial aircraft of a typical 1970s/1980s design. The wing is twisted and tapered, with an aspect ratio of 7.78, a constant quarter-chord sweep angle $\Lambda_{1/4}$ of $25°$ and a leading-edge sweep angle Λ_{LE} of $28.3°$. When scaled down to wind-tunnel dimensions by a factor of 17.5, the semi-span is $1.104\,\text{m}$, including the plinth thickness of $0.019\,\text{m}$, and the MAC is $0.279\,\text{m}$. The spanwise position, η, is made dimensionless by the reference semi-span of $1.085\,\text{m}$ after subtracting the plinth thickness, $\eta = (Y - 0.019\,\text{m})/1.085\,\text{m}$, where Y denotes the spanwise co-ordinate. Far-field conditions using a hemispherical domain are applied at a distance of 25 semi-span lengths (around 90 MAC) and a symmetry boundary condition is imposed on the centre plane. The geometry is considered rigid excluding any static deformation, such that the study focusses exclusively on the inherent fluid dynamics of shock buffet. The RBC12 model has been extensively tested in the Aircraft Research Association Transonic Wind Tunnel and any static deformation is believed to have negligible influence, as discussed in [28]. This assertion, as well as the impact of the flexible wing dynamics, deserves further scrutiny in the future, as will become clearer in this paper.

5

Table 1   Flow conditions for scale-resolving simulations.

Mach number	0.801
Re_{MAC}	3.75×10^6
Angle of attack	$3.1°$
Reference temperature	$266.5\,\mathrm{K}$
Reference pressure	$66.0\,\mathrm{kPa}$
Reference density	$0.863\,\mathrm{kg\,m^{-3}}$

The scale-resolving simulations aim to reproduce the experimental aerodynamic flow field in the vicinity of buffet onset. Transition was fixed to replicate the wind-tunnel test which employed boundary-layer tripping. The transition location on the upper surface is at 10% local chord at the wing tip, 14% at the crank and 15% at the root, whilst this is constant at 5% on the lower surface. The fuselage boundary layer is tripped at $0.104\,\mathrm{m}$ aft of the nose. In the present simulations, we chose a freestream Mach number of 0.801 with a Reynolds number based on MAC of 3.75×10^6. The angle of attack was set at $3.1°$ after running a number of exploratory time-marching simulations at lower angles. To put this into context, at the wing's design Mach number of 0.8, a critical angle of attack of just above $3.0°$ was obtained from unsteady RANS simulations [43] and a global stability analysis [47] when using the Spalart-Allmaras (S-A) model for turbulence closure. The flow conditions are summarised in Table 1.

B. Overview of Experiment

Here we provide a brief summary of the wind-tunnel testing—a detailed description and analysis can be found in [28, 42]. The tests were conducted in the Aircraft Research Association Transonic Wind Tunnel which is a closed-circuit, continuous facility. The RBC12 half-model was equipped with dedicated instrumentation for this shock-buffet-focussed test campaign. Mean pressure data was obtained from 369 static pressure taps along the fuselage and wing (specifically, 95 along the fuselage, 162 on the upper surface and 112 on the lower surface), while aerodynamic forces and moments were measured with a five-component strain gauge balance. Conventional unsteady model instrumentation amounted to 27 unsteady transducers (24 on the upper surface and 3 on the lower surface), 8 accelerometers and a root strain gauge. The upper-wing surface instrumentation is shown in Fig. 1. Additionally, a DPSP system was employed acquiring data with high spatial and temporal resolution (typically 4000 frames-per-second) over almost the entire wing. Time-averaged DPSP data is within $\pm 2000\,\mathrm{Pa}$ (corresponding to $\pm 3\%$ of reference static pressure) compared to the static pressure taps. More importantly, excellent agreement between the frequency spectra from unsteady pressure transducers and adjacent pixel data was obtained, rendering this optical measurement technique suitable to analyse the unsteady surface pressure flow field with confidence.

The flow conditions reported in the experiment have been corrected for interference effects that arise from the wind-tunnel environment. Whilst it is not essential to consider these effects in incremental testing, their influence on

(a) 162 static pressure taps

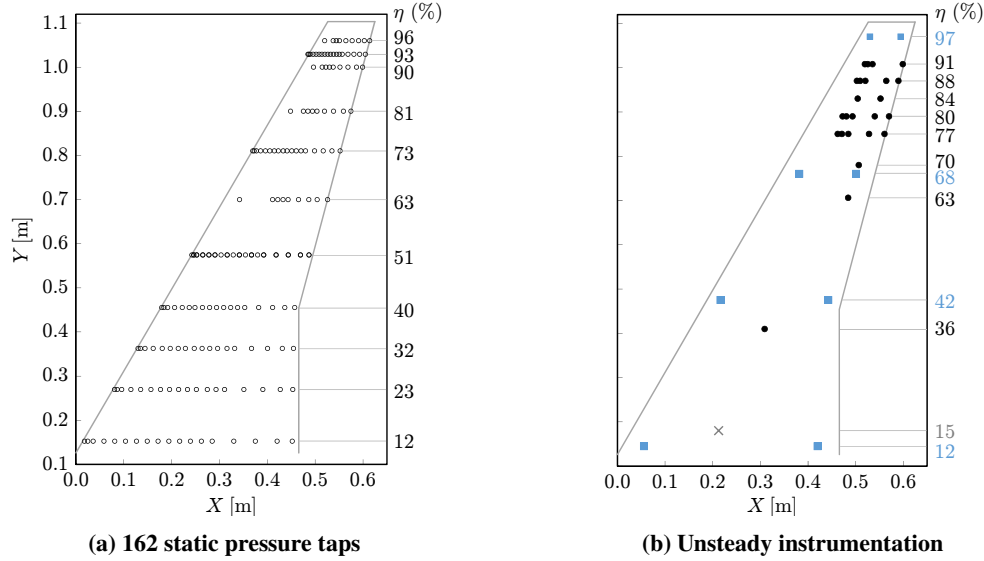**(b) Unsteady instrumentation**

Fig. 1 Model instrumentation on upper surface. Static pressure taps are indicated by open circles, whereas unsteady pressure transducers, accelerometers and a root strain gauge are given by the black filled circles, blue filled squares, and the grey cross, respectively.

flow development has to be considered when comparing to numerical simulations. The corrections applied to the experimental dataset amount to the wall constraint and paint effect, in the case of incidence, and wind-tunnel blockage for Mach number. The wall constraint correction is a function of wing span and area, lift coefficient and wall porosity, and it is given as $\Delta\alpha = -(0.6351C_L)^\circ$. The paint-effect correction is introduced to account for a thicker boundary layer due to increased surface roughness. The influence on effective aerodynamic incidence was estimated at around 0.1° by comparing pressure distributions of the painted and the unpainted model at the same flow conditions. The Mach number correction for blockage is an empirical correction based on the model's longitudinal cross-sectional area distribution and the effect of wall porosity. The calculated blockage correction is quite small, ranging between -0.01% and -0.12% of Mach number at the smallest and largest Mach numbers tested, respectively. Furthermore, the flow may also experience a small incremental angle in the vicinity of a wind-tunnel model. Direct measurement of the flow angle is restricted on half-models mounted to the floor, and an estimate of -0.35° was provided, based on several other tests comparing half models and sting-mounted full models in the same wind tunnel. At the design Mach number of 0.8, the buffet-onset incidence was found to be at $\alpha = 2.7^\circ$ using the unsteady strain-gauge signal, directly measuring the model's structural response. Herein, values for experimental data include the corrections outlined above but exclude the flow angle estimate of -0.35°, since the latter could not be directly measured, unless otherwise stated.

C. Computational Mesh

A hybrid mesh was produced using the SOLAR mesh generator [48] generally following industry best-practice guidelines [49]. The mesh consists of hexahedral-, prism- and tetrahedral-type elements and was highly refined to
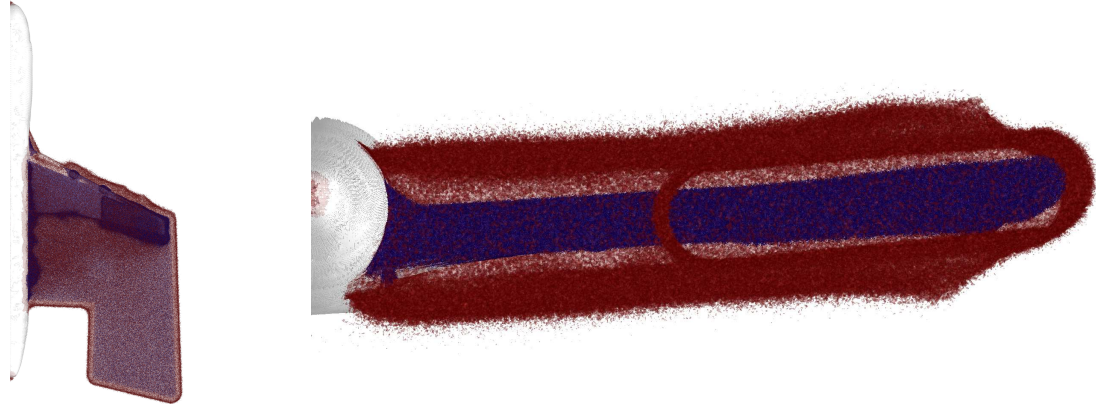
7

Fig. 2 Mesh iso-volumes highlighting refinement due to LES mesh sources. Highly-refined elements with volume 5×10^{-9} m^3 are shaded in blue, while larger elements with 5×10^{-8} m^3 are shaded in red.

resolve the turbulent structures in the separated zone. The first cell height is defined to have a y^+ of around 0.5, such that wall functions are not used. Overall there are approximately $n = 50 \times 10^6$ points with 200×10^6 elements.

As depicted in Fig. 2, two large mesh sources for the LES focus region were added to the standard meshing sources routinely used on complex wing geometries. The first source extends from 60% semi-span to just outboard of the wing tip in a spanwise sense and from just aft of the leading edge to around 4 MACs downstream of the trailing edge in the chordwise direction. In this region, the surface elements have a target spacing of $\Delta_0 \approx 0.003$ MAC, $\Delta_0 = \max\left(\Delta_x, \Delta_y, \Delta_z\right)$. This is the finest region in the mesh and was informed by experimental analysis [28, 42] and previous simulations [39, 47], both showing separation on this wing to occur first on outboard sections. The second source covers the inboard region, extending from the wing root to 60% semi-span, and approximately 2 MACs downstream of the crank. While elements in this region have $\Delta_0 \approx 0.007$ MAC, this source was primarily included to have a smooth transition from the highly refined outboard region in case turbulent eddies propagate inboard.

III. Methods and Tools

A. Flow Solver and Numerical Settings

Both steady-state and time-accurate simulations were performed using the finite-volume solver TAU, developed by the German Aerospace Center (DLR) and widely used in the European aerospace sector. The code solves the governing flow equations on hybrid unstructured meshes. The turbulence model of choice herein is the negative S-A model [50]. The second-order central scheme was used to discretise the inviscid fluxes of the mean flow equations in all simulations. However, whilst scalar dissipation was used for steady RANS simulations, a minimal level of fourth-order matrix-valued artificial dissipation was combined with a second-order energy conserving skew-symmetric convection operator for DDES to minimise discretisation errors (including both dissipation and dispersion) and provide sufficient numerical stability [51]. This was achieved by employing the hybrid low-dissipation low-dispersion scheme (LD2) [52], which

uses a numerical weighting function to discriminate between well-resolved vortex-dominated flow regions, treated with the LD2 scheme [53, 54], and coarser-grid regions, treated with the more dissipative and dispersive reference scheme. Low dissipation is ensured by setting the inverse fourth-order dissipation coefficient to 256 for the reference scheme and 1024 for the resolved region. Furthermore, different schemes were also chosen for the convective fluxes of the turbulence model—the first-order Roe scheme was employed for the steady RANS method while the second-order central scheme was used for DDES. Previous experience has shown that the prediction of unsteady regions is sensitive to both the choice of turbulence-model discretisation and the variant of a specific turbulence model (notably the use of a compressibility correction to the S-A model [55]). Effectively, the choices made can have an impact on the eddy-viscosity levels, which can inhibit the unsteadiness, see for instance [9, 39, 56, 57]. Gradients of the flow variables were reconstructed with a least squares approach which minimises errors in a hybrid mesh, such as those used herein.

The challenges imposed by massively separated flow at high Reynolds numbers motivated the development of the original DES formulation [58], designed to treat entire boundary layers with a RANS model and apply LES in separated flow regions. The practical use of pure LES at such conditions is not yet feasible due to its computational cost. The original idea was to have a single turbulence model functioning as a subgrid-scale model for LES in fine enough mesh regions and as a RANS model in coarser regions [59]. A grid spacing parameter, denoted subgrid length scale, was defined as $\Delta_{\max} = \max(\Delta x, \Delta y, \Delta z)$, motivated by the presence of highly anisotropic grids especially in the boundary-layer region [58]. The main drawback of the original DES formulation is its high dependency on grid spacing and its tendency to exhibit incorrect behaviour in thick boundary layers and shallow separation regions. Delayed DES [60] was developed to shield the boundary layer from LES treatment which would otherwise lower the eddy viscosity below the RANS level without resolving the turbulent content, leading to depleted Reynolds stresses and lower skin friction, ultimately causing premature grid-induced separation. This newer formulation helped to satisfy the original aim of DES, which is maintaining the RANS function in thick boundary layers while allowing the LES function after massive separation, by making the DES length scale also dependent on the solution, rather than the local grid characteristics only [61]. It should be noted that other definitions for the subgrid length scale have been defined, such as the commonly used LES filter width, $\Delta_{\mathrm{vol}} = \sqrt[3]{\Delta x\, \Delta y\, \Delta z}$ [62]. However, the definition based on grid spacing is preferred in DES due to its independence on the hybrid nature of the method. Furthermore, the state of the flow is taken into account by more recent vorticity-based definitions, which aim to reduce dependence on grid anisotropy [44].

Herein, we investigate switching between RANS and LES regions using two definitions of the subgrid length scale; the first is the classical DES choice of $\Delta_{\max}$ based on the maximum local grid spacing and the second is a vorticity-sensitive filter, denoted $\tilde{\Delta}_{\omega}$ as introduced in [63], which reduces to a maximum-edge formulation in the plane normal to the vorticity vector. This subgrid length scale, inspired by the work of [64], can detect the dominant two-dimensional character of early shear layers to promote a faster unlocking of the Kelvin–Helmholtz instability and early development of resolved turbulence, as described in [44, 63]. In addition, we employ DDES with a low-Reynolds-number correction

as defined in [60], previously used for shock buffet simulation on the RBC12 well-beyond the onset of unsteadiness [39].

Steady-state simulations employ local time-stepping to accelerate convergence in combination with a semi-implicit Backward-Euler scheme with a lower-upper symmetric Gauss–Seidel solver. In the scale-resolving time-marching simulations, the standard second-order dual-time stepping approach (using the steady-state solver for convergence in dual time) was used for temporal discretisation with a physical time-step of $1\,\mu s$. This corresponds to a CFL number of $\mathcal{O}\left(1\right)$, calculated using the grid spacing in the *focus region* (the region close to the body where separated turbulence must be well resolved) and a conservative measure of 1.5 times freestream velocity [65]. A dynamic Cauchy convergence criterion was applied for dual-time iterations, controlled by the drag coefficient with a relative error smaller than 10^{-8} within the last 20 iterations. Moreover, a minimum of 100 inner iterations was always performed such that the density residual norm converges by at least an order of magnitude.

B. Post-Processing

The simulation with the classical DES subgrid length scale (referred to as DDES I) run for a total physical time of $0.121\,s$ ($121\,000$ time steps) and is considered as a complete simulation with eighteen buffet cycles allowing statistical analysis after an initial transient phase. The total physical time of the second simulation employing the vorticity-sensitive definition (referred to as DDES II) is $0.06\,s$ ($60\,000$ time steps) comprising around twelve buffet cycles, sufficient to assess the influence of this more recent formulation. Flow-field data was collected at every 250 time steps, equating to a sampling frequency, f_s, of $4\,kHz$. A portion of the first simulation was sampled at $20\,kHz$, between $0.081\,s$ and $0.094\,s$, to investigate higher-frequency behaviour in the wake. Surface data was output at $10\,kHz$. Additionally, point data was sampled at every time-step (corresponding to a sampling frequency of $1\,MHz$) at 37 specific locations—27 of which correspond to the unsteady pressure transducers on the wind-tunnel model, described earlier in Sec. II.B, and 10 points are located in the wake along two spanwise stations at 63 and 77% semi-span. These sampling rates were chosen to resolve the dynamics of swept-wing buffet, namely large-scale shock motion and associated buffet cells in the separated region. Moreover, both qualitative and quantitative comparisons with the underlying experimental dataset are possible, including direct comparison with the unsteady surface pressure data measured with DPSP.

In addition to traditional post-processing including pressure distribution and Fourier analysis, these massive datasets were analysed using modal analysis techniques. These include proper orthogonal decomposition (POD) and dynamic mode decomposition (DMD) and are essentially purely data-driven algorithms. The flow-field data is decomposed into a set of spatio-temporal modes aiding the elucidation of the flow dynamics. POD gives a set of spatially-orthogonal modes which capture the most energetic structures in the data, ranked by the contribution in capturing fluctuations, but contain a range of time scales. In contrast, DMD identifies spatial modes each with a characteristic frequency and growth/decay rate, determined from the DMD eigenvalues. The unfamiliar reader is referred to the extensive overview of modal analysis techniques in fluid flows in [45]. Herein, these techniques are applied to both experimental and

Table 2   Summary of data analysed using modal analysis techniques.

Dataset	Type	Variable	f_s (kHz)	m	t_1 (s)	t_m (s)
Experimental	Surface (DPSP)	c_p	2	10000	0.0005	5
Numerical	Surface (DDES I)	c_p	10	906	0.0305	0.121
Numerical	Surface (DDES II)	c_p	10	501	0.05	0.1
Numerical	Field (DDES I)	c_p	4	363	0.0305	0.121
Numerical	Field (DDES I)	u	20	261	0.081	0.094

numerical datasets. The input is a set of vectors (commonly called snapshots) each consisting of n spatial points (in this case the mesh points) at each instance in time (for $i = 1, \ldots, m$). The *method of snapshots* [66] is used giving a much smaller eigenvalue problem of size $m \times m$ rather than $n \times n$. Modal decomposition is performed using the parallelised `modred` library [67] employing a vector-space approach. This eliminates the need to store all the snapshots in memory and makes it possible to process the whole dataset. Snapshots are prepared in the same way for both methods, except that the temporal mean is subtracted prior to applying POD to focus on the unsteady fluctuations. An overview of the data analysed is summarised in Table 2, where t_1 and t_m denote the physical time of the first and last snapshot, respectively. Flow variables are considered separately for the modal decomposition. Previous work has reported no considerable differences when using a combination of flow variables rather than separate ones [46].

IV. Conventional Analysis

A. Steady-State Simulations

Steady-state simulations were performed and analysed for verification and validation of the newly generated mesh and to elucidate the surface flow-field features, before running any computationally intensive time-accurate simulations. The angle of attack, α, was varied between $2.0°$ and $3.3°$ in increments of $0.1°$ while closely monitoring the convergence of the density residual norm as a possible indicator of physically unsteady flow. Good convergence of at least nine orders of magnitude was obtained up to $\alpha = 2.8°$. The density residual norm levels out beyond $\alpha = 2.9°$ and does not converge deeper than five orders of magnitude. These stagnating convergence norms suggest unsteady flow.

Surface pressures on the upper wing surface for several angles of attack are presented first. Figures 3a through 3d show the time-averaged values from the experimental DPSP dataset around buffet onset. The corresponding results from numerical steady-state simulations are depicted in Figs. 3e through 3h. The numerical surface pressure visualisations are enhanced by skin-friction lines and the boundaries of reverse-flow regions (based on streamwise velocity component) are denoted by the dashed lines. It should be noted that for any particular angle of attack, the experimental data without the flow angle correction results in a lower lift coefficient, as discussed later in relation to Fig. 9. However, the evolution of surface-flow phenomena with increasing angle of attack from pre-onset to beyond onset is similar. Essentially, trailing-edge separation confined to the outboard wing rapidly merges with the shock-induced separation bubble resulting
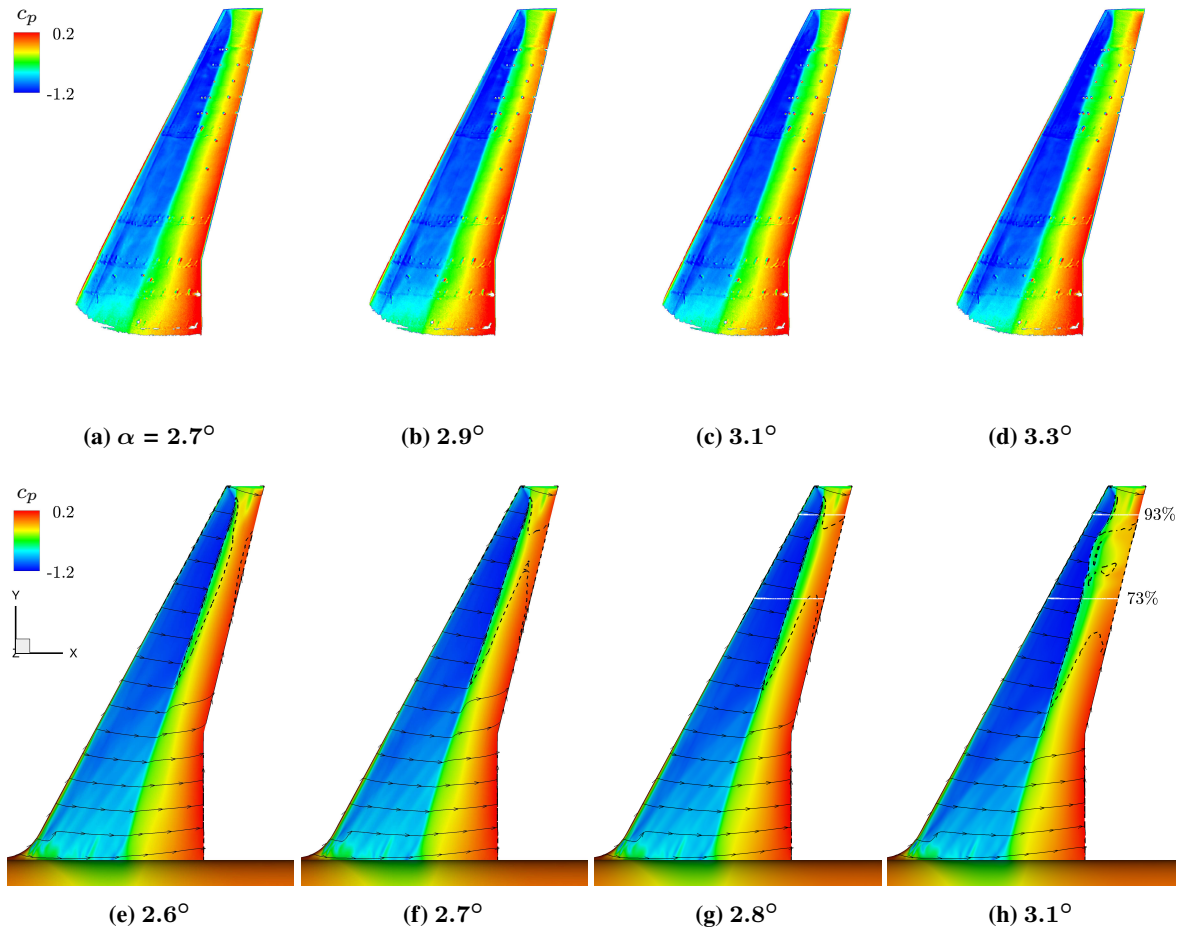
11

Fig. 3 **Comparison of surface pressure coefficient distribution from experiment and steady-state simulations at a range of angles of attack; mean surface pressure from experimental DPSP (a–d) and RANS simulations (e–h). The numerical surface flow is highlighted by skin friction lines and boundaries of reverse-flow regions are denoted by the dashed lines. Slices at 73% and 93% semi-span in (g) and (h) are further discussed in Fig. 4.**

in a region of localised separation on the outboard wing. The RANS simulations at $\alpha = 2.6°$ predict a shock-induced separation bubble which extends from mid-span and almost reaches the wing tip together with trailing-edge separation occurring between 70% and 89% semi-span. As soon as the angle of attack is slightly increased to $\alpha = 2.7°$, the incipient separation at the trailing edge starts to merge with the shock-induced separation bubble and the reverse-flow region widens with angle of attack. This corroborates the flow physics around buffet onset analysed at a wide range of Mach numbers experimentally [41, 42] and numerically [68] on the RBC12 wing. This localised separated flow perturbs the shock causing an upstream motion of the shock position with angle of attack, sometimes referred to as inverse shock motion, eventually generating spanwise oscillations visible from the shock trace at $\alpha = 3.1°$. It must be emphasised that the steady flow field is not converged beyond $\alpha = 2.9°$, and any resulting flow unsteadiness from a numerical steady-state solution scheme strictly is not time-accurate due to local time-stepping to help accelerate convergence. Caution is warranted in interpreting such findings. The shock-buffet onset incidence is further investigated
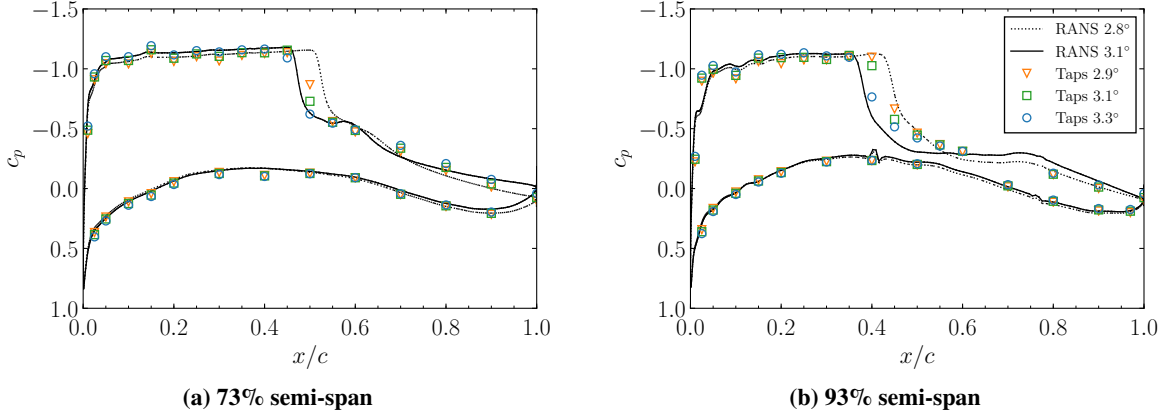
(a) 73% semi-span

(b) 93% semi-span

Fig. 4 Chordwise pressure distributions from steady-state simulations (lines) and experimental static pressure taps (symbols) at two outboard sections.

by time-marching unsteady simulations and discussed in more detail in the next section.

Steady-state chordwise pressure distributions of these RANS simulations were quantitatively assessed with respect to experimental pressure-tap data at representative spanwise locations. Pressure distributions at the two outboard stations labelled in Fig. 3h are compared in Fig. 4. The formation of a separation region and an associated upstream shock movement with increasing angle of attack can be deduced both from numerical and experimental results. At $\alpha = 3.1°$, the RANS pressure distribution at 73% semi-span clearly depicts pressure divergence close to the trailing edge, indicative of incipient separation. This is corroborated by the experimental data at 73% semi-span, whereby pressure levels are not constant between $x/c = 0.60$ and 1.0 as the angle of attack is increased from $\alpha = 2.9°$ to $3.3°$. Overall, there is closer agreement with experimental data at higher angle of attack due to the effect of a small flow angle present in the wind-tunnel flow, estimated to be around $-0.35°$, as outlined in Section II.B. Furthermore, the RANS simulations presented herein were compared favourably with solutions obtained previously using several mesh refinement levels [43, 68].

B. Delayed Detached-Eddy Simulations

The time-marching simulation using the subgrid length scale $\Delta_{\max}$ (referred to as DDES I) was initialised with a partially converged RANS solution at the same angle of attack, whilst the simulation with $\tilde{\Delta}_\omega$ (labelled as DDES II) was started from an arbitrary instantaneous flow field of DDES I at $t = 0.04\,\mathrm{s}$. A concise and intuitive overview of the numerical results together with the underlying experimental DPSP data can be found in the time-averaged surface pressure coefficient in Fig. 5 and corresponding standard deviation, σ, in Fig. 6. The choice of the experimental angle of attack ($\alpha = 3.3°$), the highest for which DPSP data is available within this study, is motivated by the resulting total lift coefficient due to the aforementioned flow angle correction, as explained below with the help of Figs. 7 and 9. From Fig. 5, it can be deduced that DDES II, compared with DDES I, results in a farther-upstream mean shock position and a
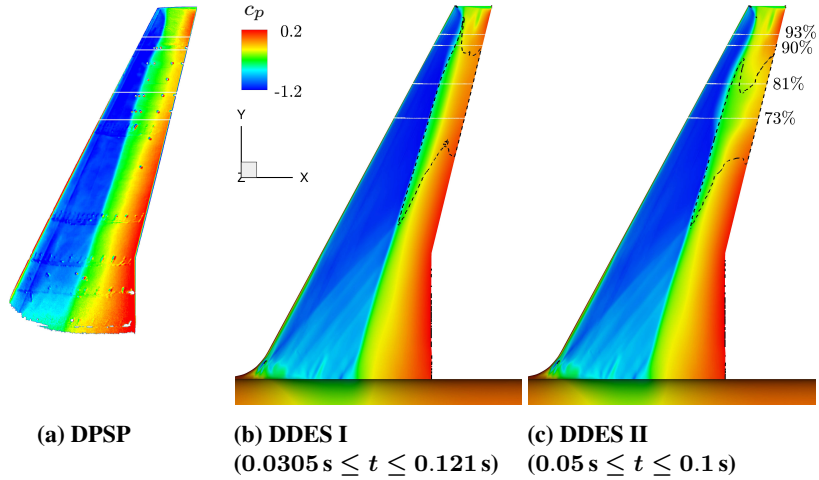
(a) DPSP **(b) DDES I** **(c) DDES II**
$(0.0305\,\mathrm{s} \le t \le 0.121\,\mathrm{s})$ $(0.05\,\mathrm{s} \le t \le 0.1\,\mathrm{s})$

Fig. 5 **Time-averaged surface pressure coefficient, evaluated within given time intervals, comparing experimental DPSP ($\alpha = 3.3°$) and DDES. Boundaries of time-averaged reverse-flow regions are denoted by the dashed lines. Slices between 73% and 93% semi-span are further discussed in Fig. 7.**
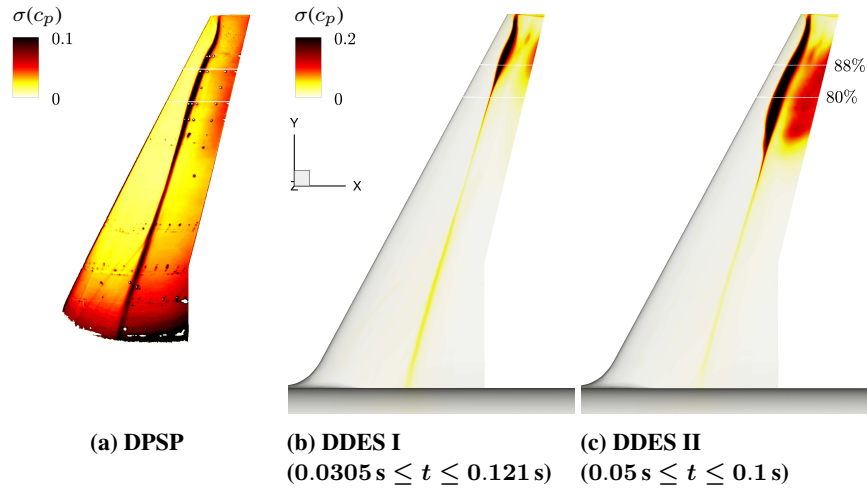

(a) DPSP **(b) DDES I** **(c) DDES II**
$(0.0305\,\mathrm{s} \le t \le 0.121\,\mathrm{s})$ $(0.05\,\mathrm{s} \le t \le 0.1\,\mathrm{s})$

Fig. 6 **Standard deviation of surface pressure coefficient, evaluated within given time intervals, corresponding to Fig. 5. Slices at 80% and 88% semi-span are further discussed in Fig. 8.**

wider separation area between approximately 70% and 90% semi-span, in closer agreement with the experimental data. These insights are reinforced by the corresponding standard deviations in Fig. 6, which additionally help assessing the level of flow unsteadiness. As expected, the bulk of unsteadiness is confined to the unsteady shock foot and the localised region of separated flow on the outboard wing. Higher levels of unsteadiness occur where resolved eddies repeatedly impinge on the wing surface along with instantaneous flow separation and reattachment. Albeit overpredicting the level of unsteadiness compared with the experimental data at $\alpha = 3.3°$, the results are promising in that the experimental angle of attack needs further increasing according to the flow angle estimate, which would result in higher values of standard deviation, cf. the experimental data in [39]. Indeed, while the work in [39] has shown that DDES (using $\Delta_{\max}$) improves
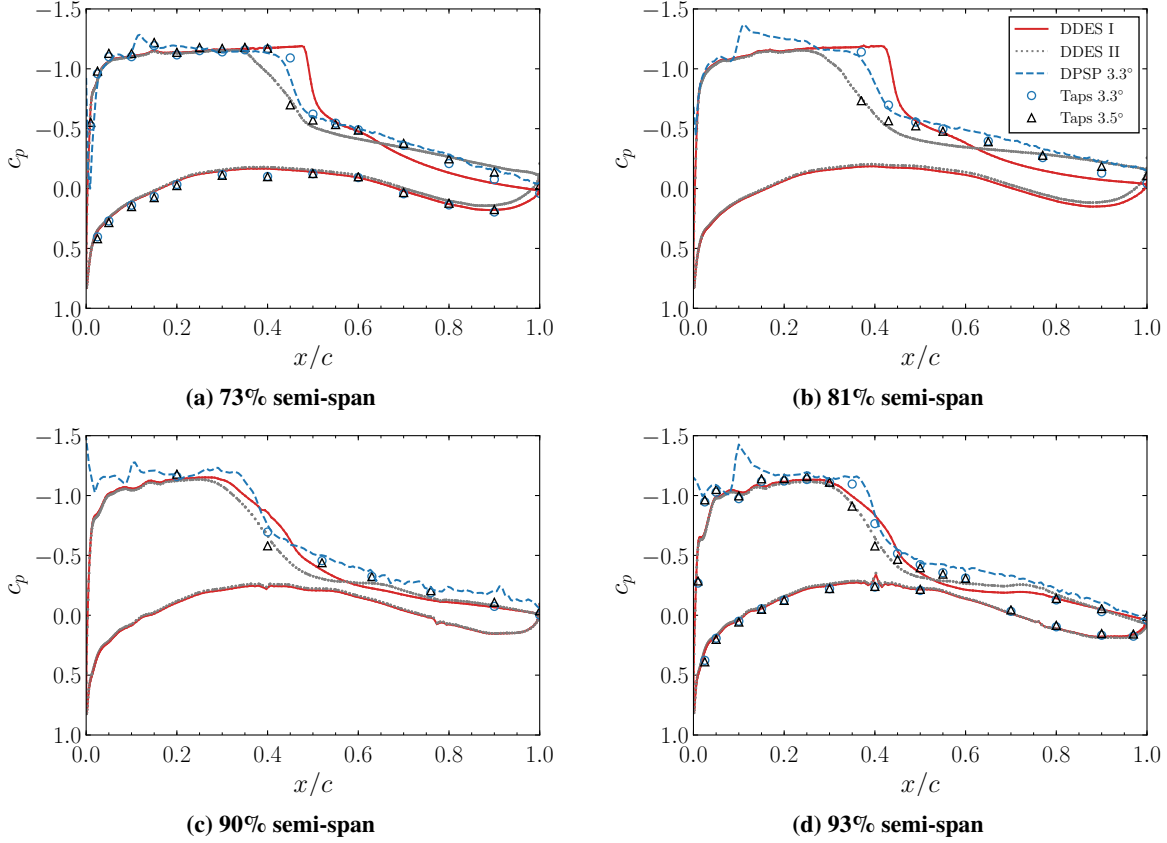
14

Fig. 7 Time-averaged chordwise pressure distributions from DDES, experimental DPSP and static pressure taps at four outboard spanwise stations.

upon unsteady RANS simulation well beyond shock-buffet onset at $\alpha = 3.8°$, here we show that the shock-induced separation near onset requires enhanced treatment for the subgrid length-scale definition, as provided by the $\tilde{\Delta}_\omega$ variant. The closer agreement between DDES II and the experimental DPSP data demonstrates how the vorticity-based subgrid length scale helps better predicting the transition from modelled to resolved turbulence in shallow shear layers. Finally, the experimental data reveals both strong unsteadiness along the shock foot extending along the whole span and highest unsteadiness inboard of the crank. While the latter is the results of measurement noise, specifically those zones lay outside the DPSP focus region, the shock unsteadiness has previously been scrutinised extensively in [42] and we will return to it in Sec. V.

A more quantitative discussion on the time-averaged surface pressures is provided in Fig. 7 presenting equivalent data at four selected outboard spanwise locations between 73% and 93% semi-span, labelled in Fig. 5c. The stations at 81% and 90% semi-span are equipped with a coarser array of pressure taps and limited to the upper surface only, cf. the instrumentation in Fig. 1. The figure compares the data from numerical DDES, experimental DPSP and static pressure taps. The impact of the flow angle correction, as explained in Sec. II.B and mentioned before, is significant. In fact, the best agreement throughout is observed between DDES II at $\alpha = 3.1°$ and the experimental data at $\alpha = 3.5°$, which is
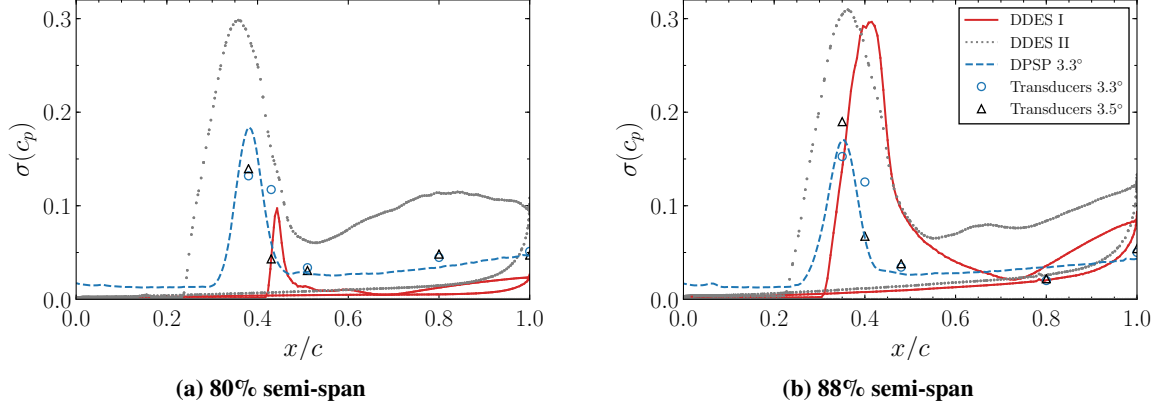
Fig. 8 Chordwise distributions of the standard deviations of surface pressure coefficient from DDES, experimental DPSP and unsteady pressure transducers at two outboard stations.

indeed very close to the corrected angle of attack due to the flow angle estimate. Two points should be noted. First, the spike in the time-averaged DPSP data at $x/c \approx 0.1$ is an artefact of the transition strip, which is also noticeable in Fig. 5a. Second, the DPSP measurement uncertainty relative to static pressure taps translates to mean $c_p \pm 0.06$.

These observations are corroborated by quantitatively comparing the standard deviations of surface pressure coefficient at the locations highlighted in Fig. 6 and presented in Fig. 8. Multiple data sources are combined, including numerical DDES, experimental DPSP and unsteady pressure transducers at two outboard spanwise stations equipped with five discrete sensors each. Numerical data is from upper and lower surfaces while experimental data has been limited to the former. Considering the complexity of the experimental and numerical setups, together with the required processing of data from disparate sources, there is remarkable agreement between experimental DPSP and DDES II, especially for the shock position, albeit a general trend in overpredicting levels of unsteadiness compared with the DPSP data, previously observed in [39]. Such processing includes the alignment and calibration of camera images against pressure taps [28], coordinate-measuring-machine readings of experimental instrumentation and the translation to extract numerical data at the corresponding locations, and the conversion of image pixel indexes to spanwise and chordwise coordinates, using the crank and wing tip, and the leading and trailing edge as reference locations, respectively. The comparisons between the two DDES distributions of both the time averages and standard deviations of surface pressure coefficient clearly show that the shock is consistently located farther upstream in DDES II, with differences particularly distinct at the two inboard stations in Fig. 7. This consequently results in a lower lift coefficient, as discussed next.

Integration of the distributed surface loads gives various integrated quantities; specifically we give detail for the lift coefficient C_L. Numerical and experimental data of the lift coefficient over angle of attack is provided in Fig. 9. Experimental data was measured with a five-component strain-gauge balance and two sets of data are shown in the figure. Points denoted by filled circles have been corrected for the interference effects described in Section II.B. Open circles additionally include an estimated flow angle correction of $-0.35°$. Numerical data from steady-state RANS
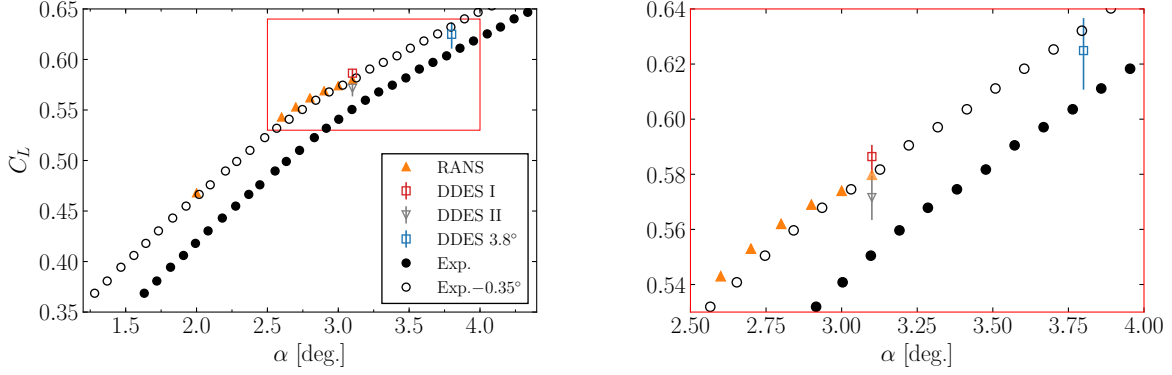
Fig. 9 Lift coefficient over angle of attack comparing experiment (open circles include flow angle correction whilst filled circles exclude it) and CFD (vertical line denotes minimum and maximum of time fluctuations). Results at $\alpha = 3.8°$ are taken from [39].

and scale-resolving simulations are presented. The latter show both the time-averaged values and the minimum and maximum fluctuations over time, denoted by the vertical lines. There is good correlation between numerical and experimental data when the flow angle correction is included, giving confidence in the numerical simulations overall. Data from DDES I and II together with a previous simulation at $\alpha = 3.8°$, reproduced from [39], are included. Focussing on the simulations at $\alpha = 3.1°$, DDES I undergoes lift fluctuations of approximately ±0.005 around the mean value, while DDES II has bigger fluctuations of approximately ±0.008, in agreement with the level of unsteadiness as presented in Fig. 6a. The unsteady flow physics corresponding to these fluctuations are described in more detail in Sec. V.

Time-resolved histories of the lift coefficient were monitored and analysed for two main reasons. First, a transient phase, when high eddy-viscosity regions arising from the steady RANS formulation are destroyed by the less dissipative DDES method, can be identified until the flow develops self-sustained unsteadiness. Second, the frequency content of the fluctuations can be studied, which is useful considering that one of the main differences between aerofoil and swept-wing shock buffet is the spectral signature of the aerodynamic loads. Power spectral density (PSD) data was estimated using Burg's method [69] to assess the frequency content of the lift fluctuations. This autoregressive model was selected since it provides high frequency resolution even for short signals, typical for such time-accurate simulations. The autoregressive PSD estimation was computed with a single window and an order of 4000 after conducting a parametric study (not shown herein).

Lift-coefficient time histories from three scale-resolving simulations are shown in Fig. 10. These include the two current simulations in the vicinity of buffet onset together with a previous DDES at a higher angle of attack $\alpha = 3.8°$, well-beyond buffet-onset conditions. Those latter results, which used the Δ_{max} subgrid length scale, were reproduced from [39]. Their corresponding PSD data are depicted in Fig. 11. Previous numerical studies, as explained in Section II.A, found the critical angle of attack to be just above $\alpha = 3.0°$. Short, exploratory time-marching simulations were conducted starting at $\alpha = 2.9°$ in increments of $\Delta\alpha = 0.1°$, based on the indication of physically unsteady flow
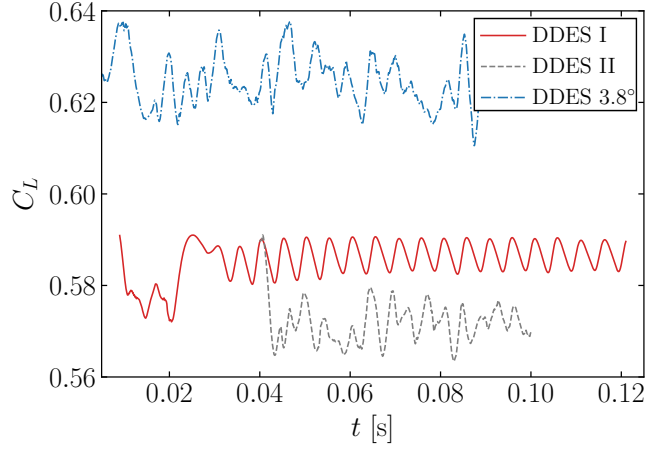
Fig. 10   Time history of lift coefficient. Results at $\alpha = 3.8°$ are reproduced from [39].
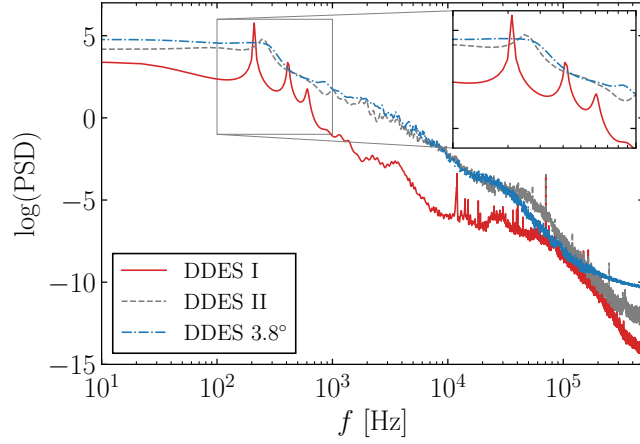

Fig. 11   Power spectral density data of lift-coefficient histories in Fig. 10.

from the stagnating steady-state convergence. Self-sustained lift fluctuations due to the shock-buffet phenomenon were only observed at $\alpha = 3.1°$ and it was hence decided to pursue the production runs at this angle of attack. An initial transient phase can be observed in the time histories in Fig. 10, upon starting the simulations. Following this start-up, specifically $t > 0.0305\,\mathrm{s}$ for DDES I and $t > 0.05\,\mathrm{s}$ for DDES II, the complete signal, unless otherwise stated, has been considered as developed shock buffet and is used for the signal processing and subsequent analysis. DDES I results are characterised by fairly regular periodic lift fluctuations caused by an oscillating shock perturbed by a pulsating separation bubble, and vice versa, as discussed in detail later. DDES II, using a more recent, vorticity-sensitive subgrid length scale, yields more intense and less regular lift fluctuations, possibly owing to a wider spanwise separation region and the action of resolved turbulence. Moreover, the average lift coefficient is lower as the mean shock position shifts farther upstream compared to DDES I, as discussed earlier. The scale-resolving simulation at $3.8°$ has a more irregular time-history yet together with larger-amplitude fluctuations around a higher average value. With regards to the

18

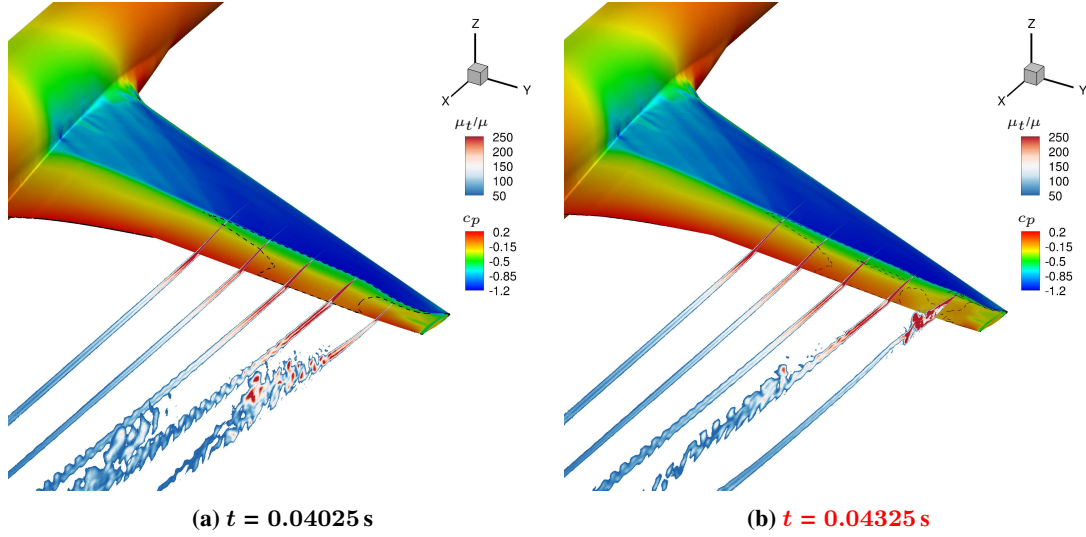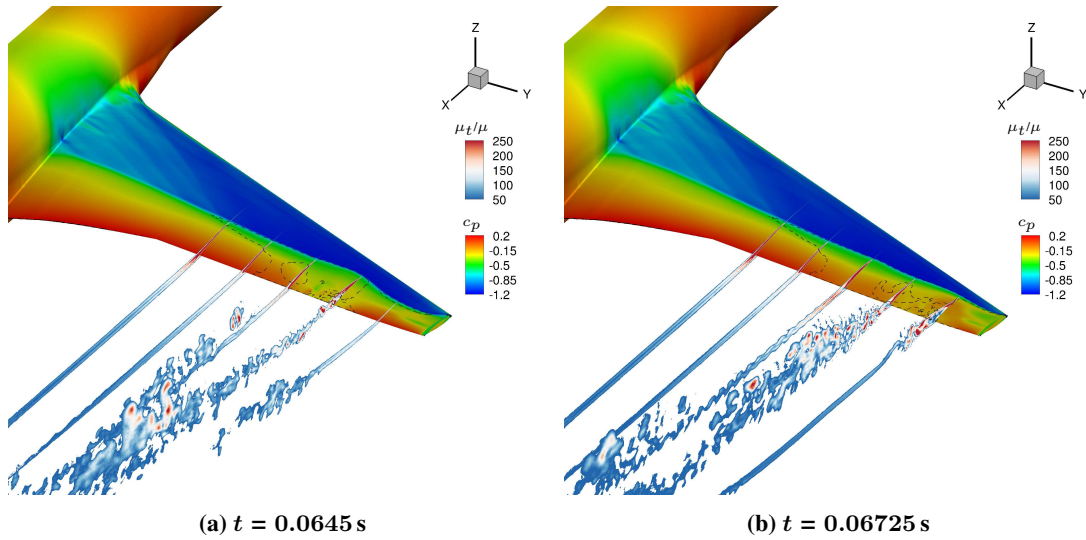**(a)** $t = 0.04025\,\mathrm{s}$ **(b)** $t = 0.04325\,\mathrm{s}$

Fig. 12   Instantaneous surface pressure coefficient and reverse-flow region (denoted by dashed lines) together with slices of eddy-viscosity ratio (μ_t/μ) both during a high-lift and low-lift phase at $\alpha = 3.1°$ from DDES I.

(a) $t = 0.0645\,\mathrm{s}$ **(b)** $t = 0.06725\,\mathrm{s}$

Fig. 13   Instantaneous surface pressure coefficient and reverse-flow region (denoted by dashed lines) together with slices of eddy-viscosity ratio (μ_t/μ) both during a high-lift and low-lift phase at $\alpha = 3.1°$ from DDES II.

frequency content shown in Fig. 11, a clear peak at approximately $200\,\mathrm{Hz}$ (corresponding to $St = 0.22$) together with its harmonics characterise the spectrum from DDES I, as expected from the underlying time history. The dominant peaks are less well defined in DDES II and the simulation at $\alpha = 3.8°$ due to the irregular nature of the fluctuations. A bump centred at approximately $f = 245\,\mathrm{Hz}$ ($St = 0.27$) is evident from DDES II results.   These frequencies are compatible with typical values reported for swept-wing shock buffet [22, 25, 26].

In order to judge the resolved turbulent content from the scale-resolving simulations, Figs. 12 and 13 present instantaneous surface pressure distributions together with slices of eddy-viscosity ratio, μ_t/μ, (i.e. the ratio of turbulent-

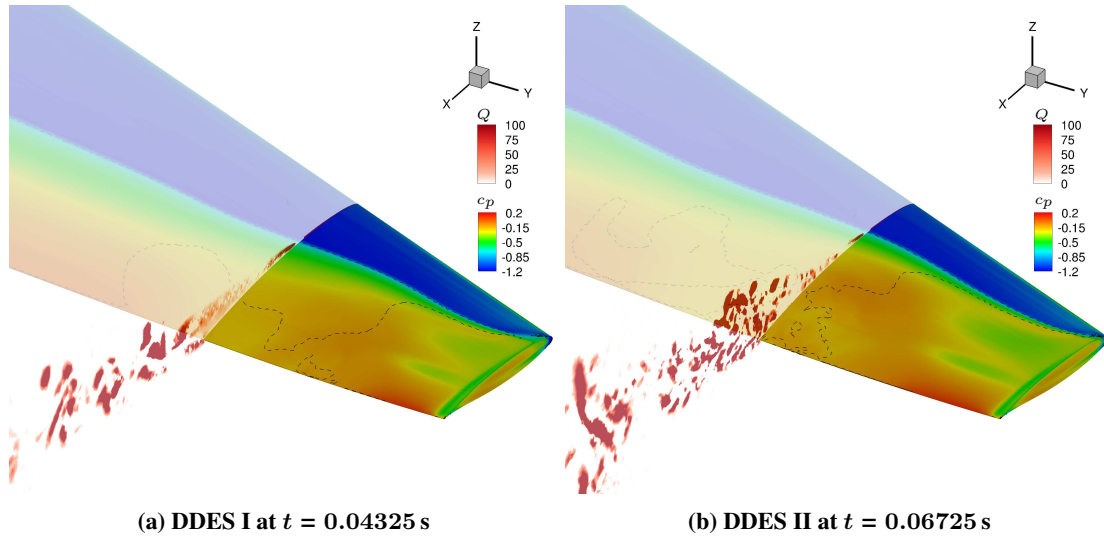**(a) DDES I at $t = 0.04325\,\text{s}$**   **(b) DDES II at $t = 0.06725\,\text{s}$**

Fig. 14   Instantaneous surface pressure coefficient and a representative slice at 86% semi-span showing dimensionless Q-criterion during a low-lift phase. Dashed lines denote the reverse-flow region.

to-laminar viscosity) for DDES I and DDES II, respectively. The snapshots correspond to instances during both a high-lift and a low-lift phase, as seen in Fig. 10. The slices are between 50% and 90% semi-span in 10% increments. The highly-refined region encapsulating the outboard wing allows for LES treatment and resolved turbulent content is depicted in the outboard slices. During a shock-buffet cycle, intermittent pockets of shock-induced separation appear predominantly during a local upstream position in the shock oscillation (corresponding to a low-lift phase and hence troughs in the lift history), which is benevolent to the generation of resolved content downstream of the shock. Comparing the results from DDES I and DDES II allows two conclusions. First, the slices from DDES II indicate lower levels of the eddy-viscosity ratio implying more resolved content. Second, an accelerated transition from RANS to LES is visible when applying the vorticity-sensitive formulation in DDES II, resulting in more resolved turbulent content starting in the shear layer above the wing and consequently more content in the wake closer to the wing. This is also evident from Fig. 14 which depicts the Q-criterion at a representative outboard slice at 86% semi-span during a low-lift phase. While the results from DDES I indicate significant release of stronger turbulent eddies aft of the trailing edge, an observation which contributes to the more regular lift oscillations as seen in Fig. 10, this transition to resolved content is moved upstream for DDES II, taking place more gradually.

V. Data-Based Modal Analysis

A detailed investigation into the underlying experimental dataset [42] has identified two coexisting phenomena—a low-frequency shock unsteadiness along the whole span centred at approximately $70\,\text{Hz}$ (corresponding to $St \approx 0.07$), which propagates pressure in the inboard direction towards the root, together with higher-frequency outboard-running perturbations at $> 200\,\text{Hz}$ (corresponding to $St > 0.22$) confined to the outer wing region. Previous work employing

numerical time-linearised analysis [47] similarly pointed out distinct flow responses. Specifically, forced wing vibration excited a low-frequency response, dominated by shock unsteadiness but with low sensitivity to angle-of-attack increments in the vicinity where self-sustained flow unsteadiness is first observed, and higher-frequency peaks typical for swept-wing shock buffet that are greatly amplified around critical conditions. The latter has been linked to globally unstable and weakly damped eigenmodes [40], whereas the former bears similarity to a long-wavelength inboard-running eigenmode identified for a simplified infinite-wing geometry [34]. Nevertheless, while some consensus has emerged in recent years concerning the swept-wing shock-buffet modes and associated buffet cells, questions remain in relation to the lower-frequency behaviour.

In this regard, our time-accurate simulations were analysed using data-based modal analysis techniques to provide a spatio-temporal representation of the dominant coherent flow features. The discussion starts with an analysis of surface pressure data both from experimental DPSP and DDES. This is followed by an analysis over the whole computational domain. We identify modes related to shock buffet and coherent medium-frequency shear-layer structures.

A. POD Surface Analysis

POD analysis was conducted on the experimental DPSP data and the two DDES simulations. The spatial component of dominant POD modes both from experimental and numerical surface pressure coefficient data is depicted in Fig. 15, highlighting the dominant flow features responsible for the largest fluctuations. Each POD mode has unit norm and the highest spatial amplitudes occur along the unsteady shock and the region farther downstream. The spatial amplitudes represent positive or negative perturbations around the mean pressure value, depending on their sign and the corresponding temporal coefficient (there are as many temporal coefficients as snapshots denoting the time evolution of each POD mode at every spatial point). To illustrate, at a positive temporal coefficient, regions of higher and lower pressure are depicted by positive (red) and negative (blue) spatial amplitudes, respectively. Focussing on the experimental data, the shock sits upstream of its mean position on the outboard wing inducing flow separation. Farther inboard, the shock is downstream and the flow remains attached. The dominant mode from DPSP corresponds to a low-frequency inboard-running behaviour. The unsteadiness obtained numerically is confined to the outboard region, with that from DDES II covering a wider spanwise region, corroborating the observation made for standard deviation in Fig. 6. In contrast to the experimental mode, the numerical modes have an outboard-running behaviour. Another example of a resulting POD mode is depicted in Fig. 16 from which similar observations can be made. Experimentally, since several intermediate modes are related to the wing's structural response, mode 8 is shown instead in Fig.16a—the first one, ranked by POD energy, to capture the shock rippling on outboard sections and causing pockets of shock-induced separation that follow the upstream shock excursions. In the case of numerical data, the spatial components of mode 2 are shown, with DDES II resulting in remarkable agreement with the experimental data.

To obtain the temporal behaviour of these modes, PSD data based on the temporal coefficients corresponding to the
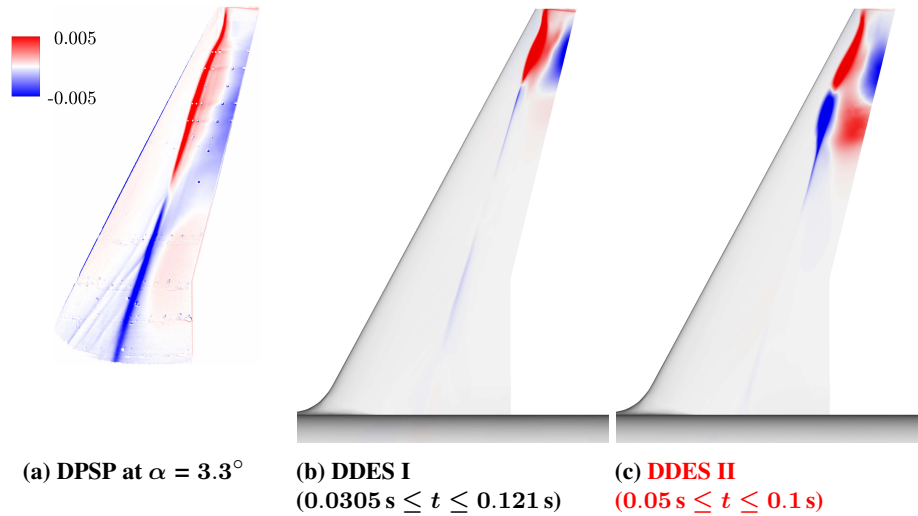
21

(a) DPSP at $\alpha = 3.3°$

(b) DDES I
($0.0305\,\mathrm{s} \leq t \leq 0.121\,\mathrm{s}$)

(c) DDES II
($0.05\,\mathrm{s} \leq t \leq 0.1\,\mathrm{s}$)

Fig. 15   Spatial component of dominant POD mode 1 from DPSP and DDES surface pressure coefficient data, coloured by spatial amplitudes.

(a) DPSP at $\alpha = 3.3°$

(b) DDES I
($0.0305\,\mathrm{s} \leq t \leq 0.121\,\mathrm{s}$)

(c) DDES II
($0.05\,\mathrm{s} \leq t \leq 0.1\,\mathrm{s}$)
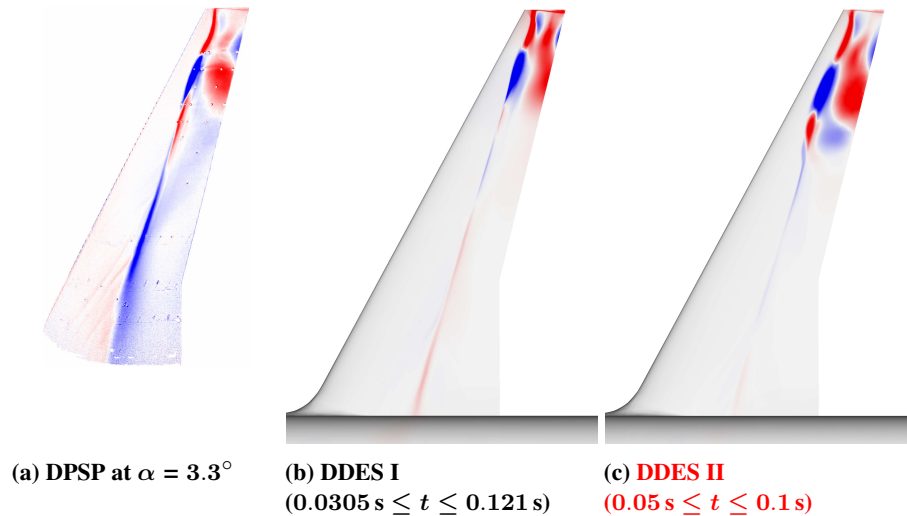
Fig. 16   Spatial component of a less dominant POD mode from DPSP (mode 8) and DDES (mode 2) surface pressure coefficient data. Contour levels correspond to Fig. 15.

modes presented in Figs. 15 and 16 are shown in Fig. 17. Power spectra of the DDES signals was computed using Burg's method [69], whilst Welch's method [70] was chosen for the longer DPSP signal. In all cases, the spectra were normalised by their respective maximum value. Considering the DPSP dataset, mode 1 is centred at lower frequencies around 70 Hz, typical of the inboard-running low-frequency shock unsteadiness [42], whereas mode 8 shifts to a higher frequency above 200 Hz that is characteristic of the outboard-propagating shock-buffet instability. Temporal fluctuations of modes 1 and 2 from DDES I show a clear peak at 200 Hz, matching the primary peak obtained from the lift coefficient in Fig. 10, while lacking the broadband content observed experimentally. This broadband content appears in the PSD
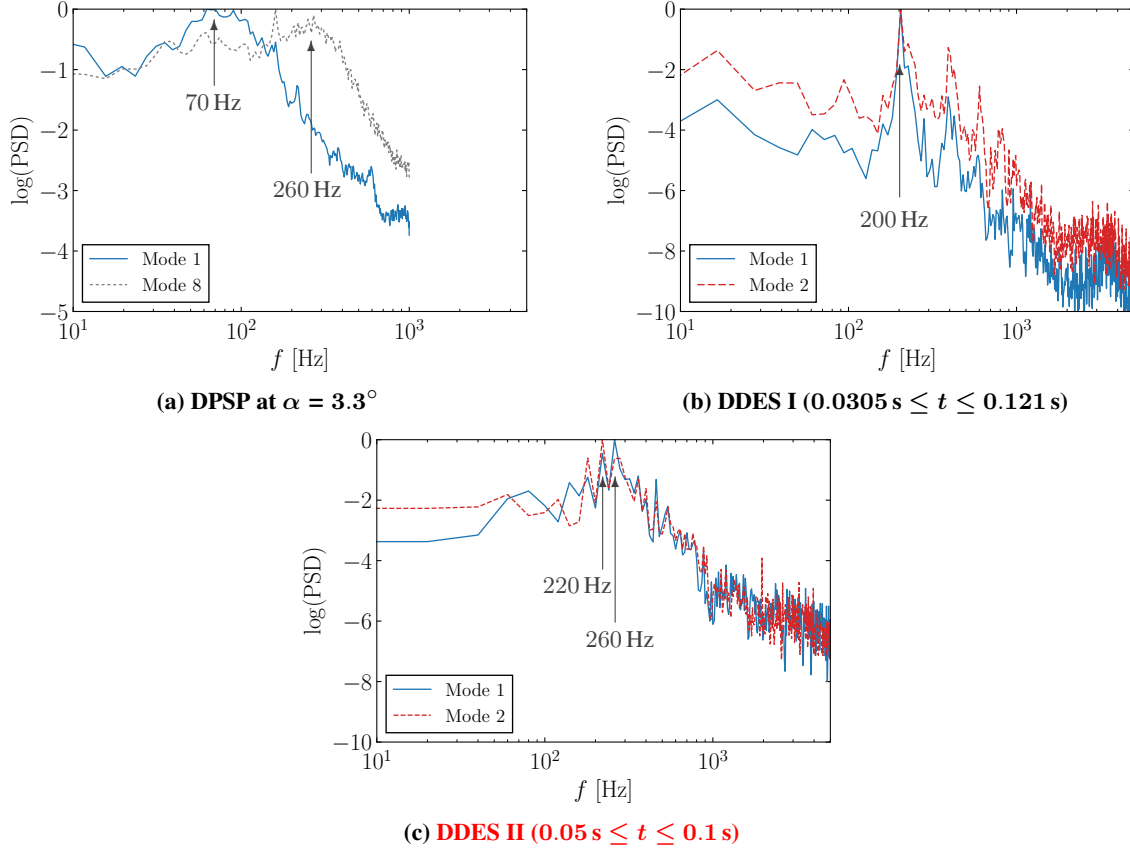
(a) DPSP at $\alpha = 3.3°$

(b) DDES I ($0.0305\,\text{s} \le t \le 0.121\,\text{s}$)

(c) DDES II ($0.05\,\text{s} \le t \le 0.1\,\text{s}$)

Fig. 17   PSD data of POD temporal coefficients for modes shown in Figs. 15 and 16.

data from DDES II, peaking at $220\,\text{Hz}$ ($St = 0.23$) and $260\,\text{Hz}$ ($St = 0.28$) and lying within the range of the spectral bump from the lift fluctuations. Together with the observed spatial variations in Figs. 15c and 16c, the broadbandedness can be explained. Similar to the spatial amplitudes, the agreement with the experimental mode 8 is striking.

B. DMD Surface Analysis

DMD was applied to the surface pressure snapshots to extract dynamic information and to isolate the flow phenomena based on frequency. Whilst in POD the modes are naturally ranked by the fluctuation energy, DMD mode sorting is less obvious. Herein, spectral coefficients are computed as the norm of the first projection coefficient, analytically equivalent to the least-squares projection of the first snapshot onto a projected DMD mode. To take into account the time evolution of each DMD mode, the spectral coefficients are scaled by the absolute value of the corresponding eigenvalue to promote growing and slowly-decaying modes, while reducing the peaks of modes with a large norm but of quickly-decaying nature [71]. The resulting DMD spectra from DPSP and the simulations are shown in Fig. 18, where the spectral coefficients are normalised by the maximum value, excluding that of the mean-flow mode. The dominant DMD mode from DDES I has a frequency of $197\,\text{Hz}$ ($St = 0.22$) whereas that from DDES II is $278\,\text{Hz}$ ($St = 0.30$). In the latter case, the spectrum is more broadband and DMD modes at $199\,\text{Hz}$ ($St = 0.22$) and $237\,\text{Hz}$ ($St = 0.25$)

23

(a) **DPSP at $\alpha = 3.3°$**

(b) **DDES I ($0.0305\,\text{s} \leq t \leq 0.121\,\text{s}$)**

(c) **DDES II ($0.05\,\text{s} \leq t \leq 0.1\,\text{s}$)**
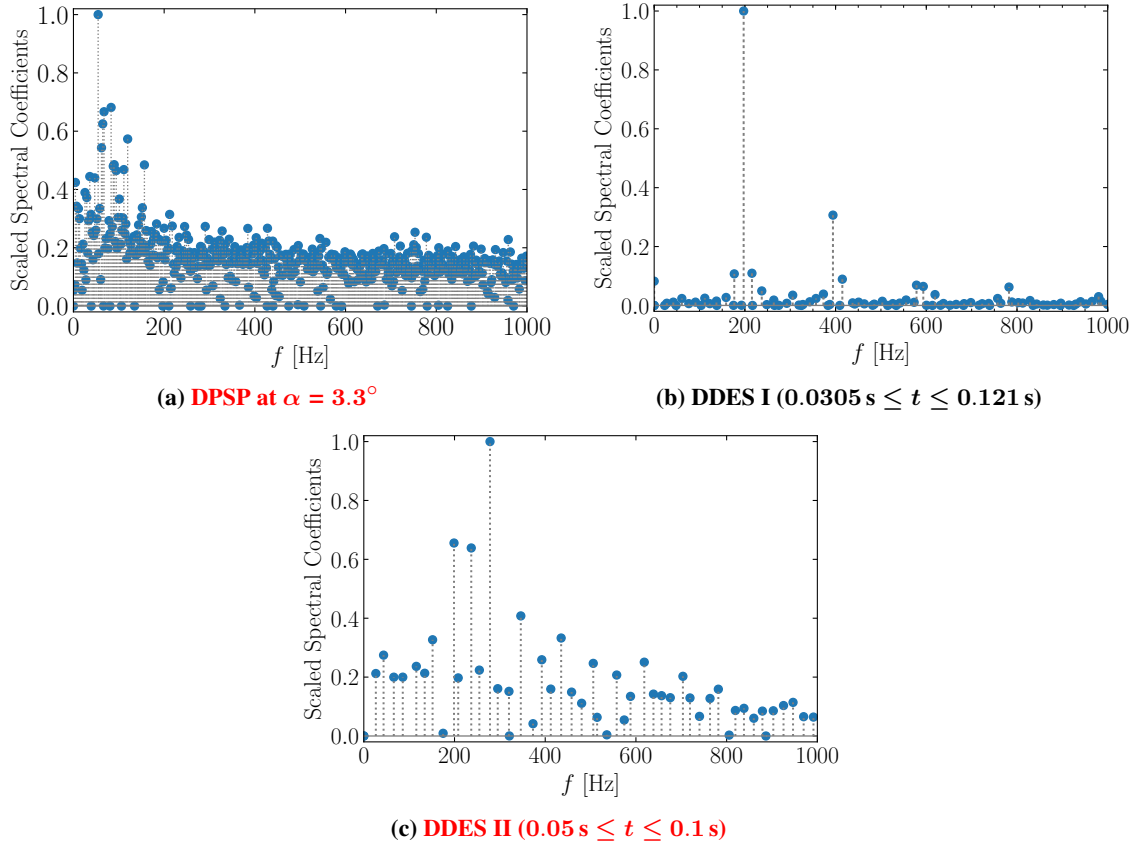
Fig. 18   DMD spectrum for surface pressure snapshots from DDES and DPSP.

also have relatively high contributions. All these three modes look very similar when visualised. In the case of the experimental data, the spectrum is broadband with a large number of modes since the number of input snapshots is higher. The dominant modes lie within the low-frequency shock unsteadiness range [42] which is not captured by the DDES. However, visualisation of the modes within the higher-frequency range ($0.2 \leq St < 0.5$) reveals the highest contribution along the outboard shock with propagation towards the tip, similar to the simulations, as shown next.

Each DMD mode is a complex-valued spatial field scaled to unit norm. The spatial amplitudes on the wing surface of both real and imaginary parts for selected modes are depicted in Figs. 19 through 21. In addition, the corresponding magnitude and phase are also included. It is evident that the DMD modes from DDES with the highest spectral coefficient are very similar to POD modes 1 and 2, presented previously in Figs. 15 and 16. Variations between the real and imaginary parts provide information regarding the pressure propagations and clarify the dynamics at a single frequency of interest. This is the added insight that DMD provides to the analysis. The magnitude of the complex numbers highlights the intensity of pressure perturbations while the phase variation indicates the direction of propagation. A comparison of the magnitude of the dominant DMD modes in Figs. 19c through 21c immediately elucidates pressure perturbations that are confined closer to the wing tip. The shock dynamics are similar in both
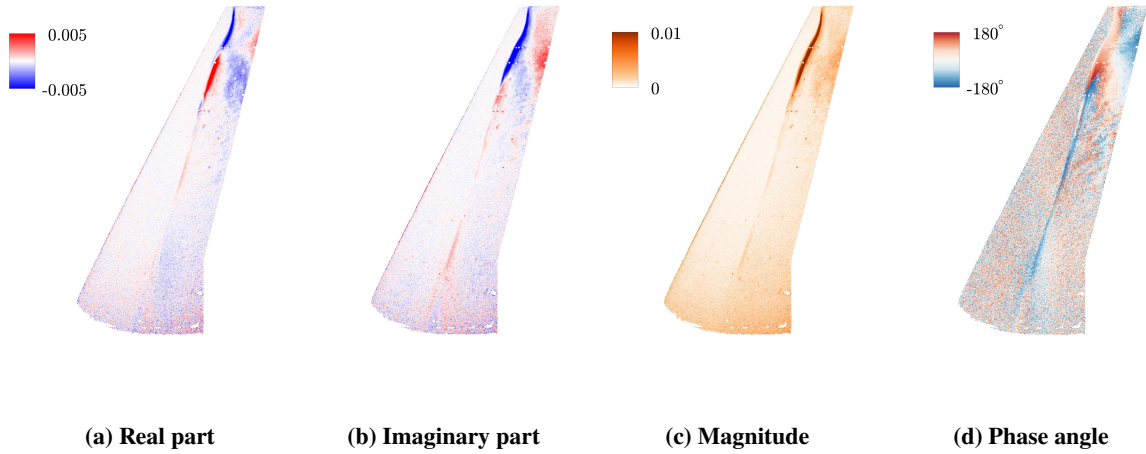
(a) Real part   (b) Imaginary part   (c) Magnitude   (d) Phase angle

Fig. 19   **Dominant DMD mode from experimental DPSP ($\alpha = 3.3°$) with frequency of 245 Hz.**

(a) Real part   (b) Imaginary part   (c) Magnitude   (d) Phase angle
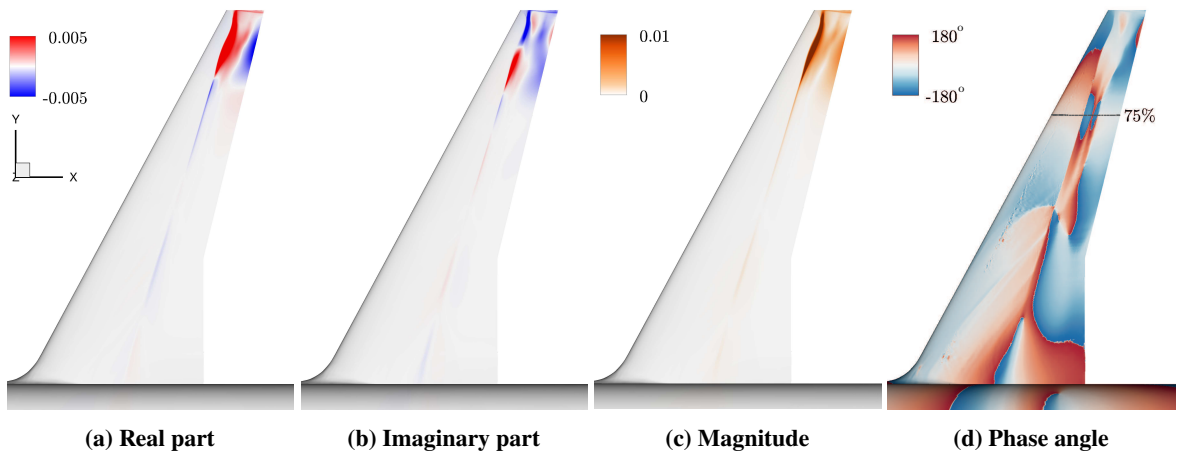
Fig. 20   **Dominant DMD mode from DDES I ($0.0305\,\text{s} \leq t \leq 0.121\,\text{s}$) with frequency of 197 Hz.**

(a) Real part   (b) Imaginary part   (c) Magnitude   (d) Phase angle
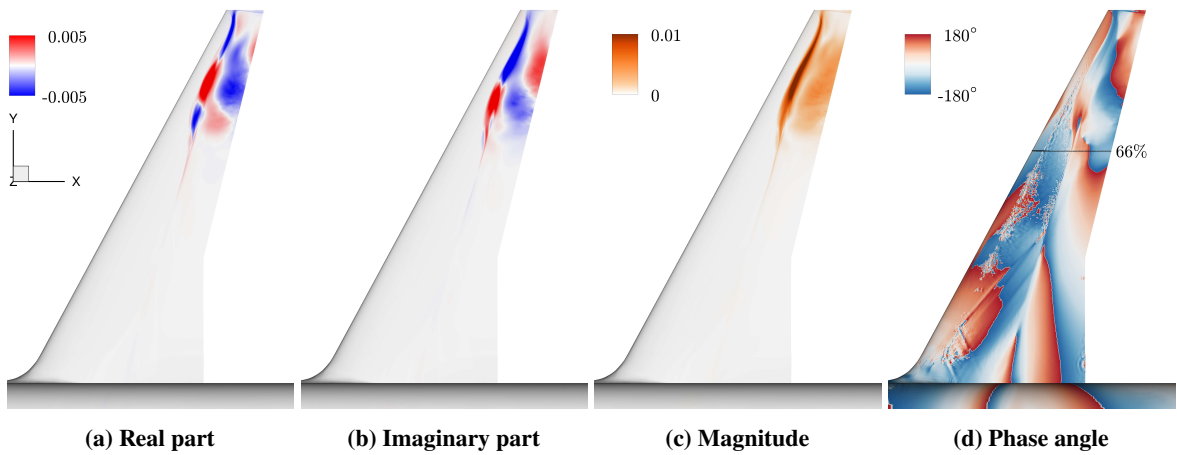
Fig. 21   **Dominant DMD mode from DDES II ($0.05\,\text{s} \leq t \leq 0.1\,\text{s}$) with frequency of 278 Hz.**

(a) POD mode 1   (b) DMD mode (ℜ) 197 Hz   (c) DMD mode (ℑ) 197 Hz
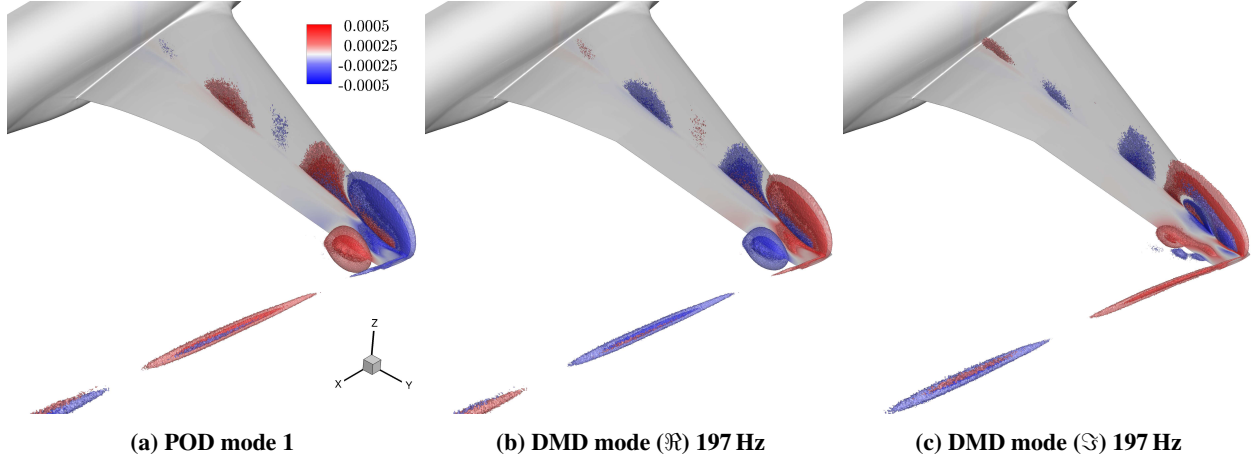
Fig. 22   **Dominant modes from DDES I ($0.0305\,\text{s} \le t \le 0.121\,\text{s}$) showing field pressure coefficient data visualised by iso-surfaces of the spatial amplitudes.**

(a) $f_s = 4\,\text{kHz}$ ($0.0305\,\text{s} \le t \le 0.121\,\text{s}$)   (b) $f_s = 20\,\text{kHz}$ ($0.081\,\text{s} \le t \le 0.94\,\text{s}$)
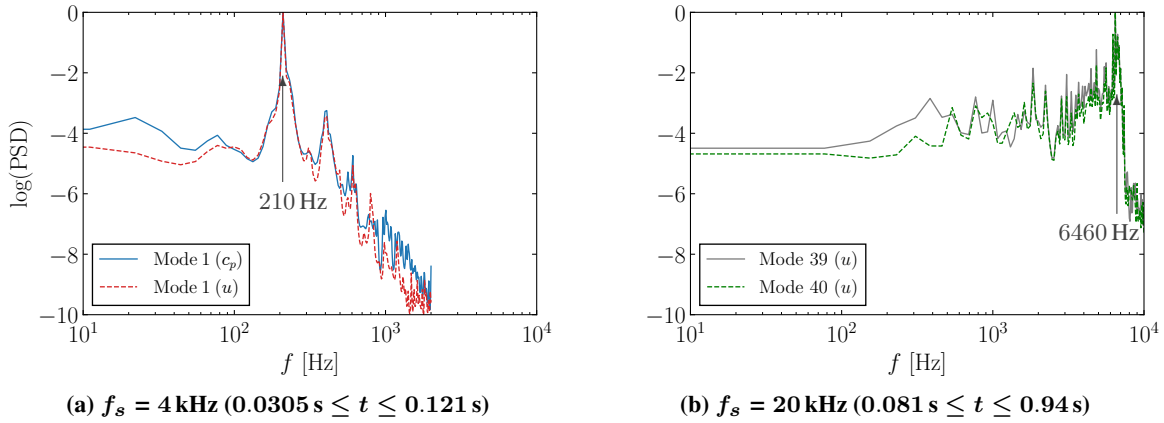
Fig. 23   **Normalised PSD data of POD temporal coefficients of shock-buffet and wake modes from field pressure coefficient and streamwise velocity data.**

simulations and the experiment with the phase angle gradually decreasing in the spanwise direction along the shock (outboard of 75% semi-span in DDES I and 66% semi-span in DDES II), corresponding to pressure propagation towards the wing tip. Apparent discontinuities in the phase angle are due to phase wrapping and have no physical meaning. A phase difference of approximately π between the shock foot and the trailing edge corroborates the flow physics implied by the opposite signs of the POD spatial amplitudes in these regions, i.e. trailing-edge separation occurs when the shock is upstream of its mean position.

C. Flow-field Analysis

Complete field data from the longer DDES I simulation was decomposed using both POD and DMD. Figure 22 depicts the spatial structures of dominant modes from pressure coefficient data, corresponding to the surface pressures shown in Figs. 15b and 20. Very similar spatial structures comparing POD and DMD were obtained from the real part of
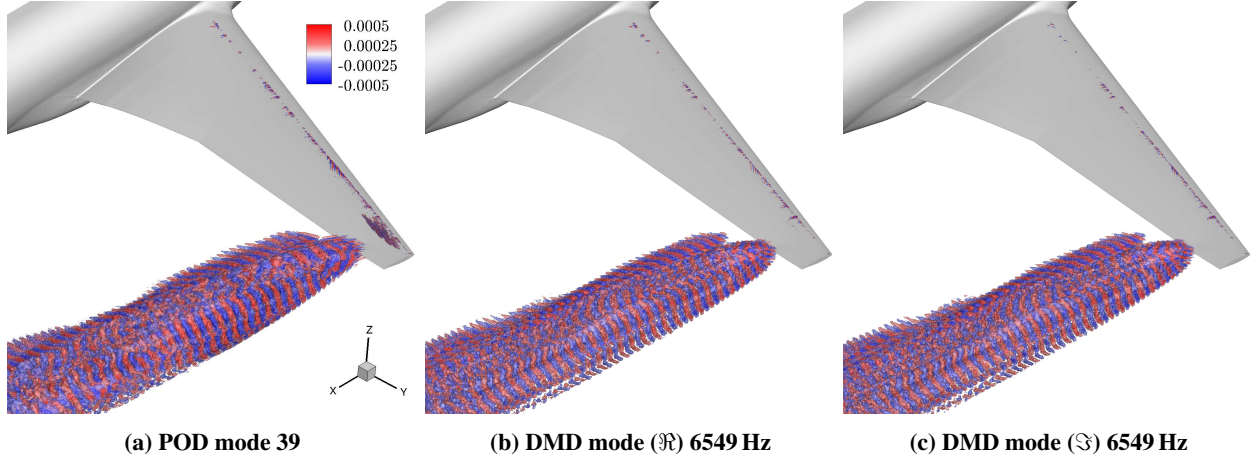
(a) POD mode 39   **(b) DMD mode ($\Re$) 6549 Hz**   **(c) DMD mode ($\Im$) 6549 Hz**

Fig. 24   Coherent mode identified from streamwise velocity data u of DDES I ($0.0305\,\mathrm{s} \leq t \leq 0.121\,\mathrm{s}$) visualised by iso-surfaces of the spatial amplitudes.

the DMD mode with the highest spectral coefficient at $197\,\mathrm{Hz}$. Variations between the real and imaginary parts highlight the propagation of buffet cells towards the wing tip and into the wake. Equivalent modes from streamwise velocity and momentum data were also analysed (not shown herein) highlighting flow separation as a result of an upstream shock movement and perturbations reaching into the wake. PSD data of the temporal coefficients of the dominant POD modes presented in Fig. 23a show a peak at $210\,\mathrm{Hz}$, approximately the same as that obtained from surface data. Slight differences are due to different sampling rates. Modal analyses of the field data sampled at $20\,\mathrm{kHz}$ give the same dominant modes as those shown with a lower sampling rate.

However, the highly sampled segment, cf. Tab. 2, reveals additional modes constituting coherent structures in the shear layer as visualised in Fig. 24. These were captured by POD modes 39 and 40 which have similar spatial appearance but are temporally shifted ($90°$ out-of-phase), together describing a downstream convection. This propagation is represented by the real and imaginary parts of a particular DMD mode with a frequency of $6549\,\mathrm{Hz}$. The temporal components of POD modes 39 and 40 highlight a higher-frequency bump peaking at $6460\,\mathrm{Hz}$, as shown in Fig. 23b. For this longer and more complete DDES I simulation, data was also sampled at every physical timestep (sampling frequency of $1\,\mathrm{MHz}$) at chosen points on the wing's surface and in the wake to scrutinise resolved turbulent content. Normalised PSD data of pressure and streamwise velocity fluctuations are presented in Fig. 25 showing the two main features. First, all spectra both on the surface and in the wake are characterised by the dominant $200\,\mathrm{Hz}$ shock-oscillation frequency. Second, spectra in the wake have their highest energy content within a frequency bump centred at approximately $6550\,\mathrm{Hz}$ due to smaller-scale turbulent fluctuations, better resolved from the streamwise velocity data. It should be noted that, although these spectra show higher PSD levels farther downstream, this is an effect of normalising the PSD graphs. Indeed, the highest levels in unsteadiness can be found farther upstream in the vicinity of the shock location. This frequency peak from the point analysis is in agreement with that identified from the modal analysis. Although

(a) Static pressure
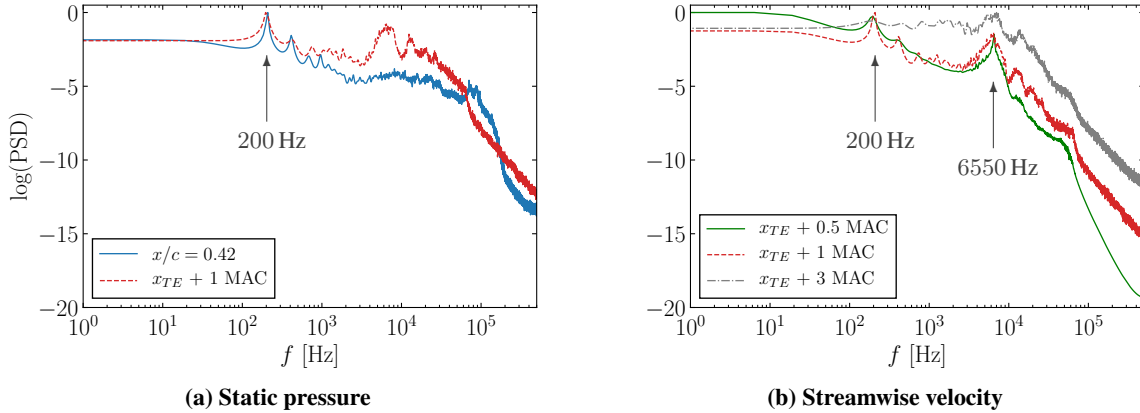
(b) Streamwise velocity

Fig. 25 Normalised PSD data of pressure and velocity fluctuations at chosen points (specifically at 77% semi-span and chordwise positions as indicated in the legend) from DDES I.

several modes capture eddies spanning the whole frequency range up to the Nyquist frequency, their spatial structures are incoherent. In contrast, modes with coherent structures have a common peak within this frequency bump. Both their spatial structures and frequency content bear similarity with a Kelvin–Helmholtz-type instability in the shear layer, which co-exists with the shock-buffet phenomenon. Similar observations were reported on aerofoils and wings in buffet flow conditions [15, 20, 26].

VI. Conclusions

In the transonic flow around a large aircraft wing geometry, two phenomena have previously been identified experimentally from an optical measurement technique, specifically dynamic pressure-sensitive paint—a lower-frequency shock unsteadiness with a wavelength almost extending along the entire span, which is also active before a root stain gauge identifies structural buffeting, and a higher-frequency cellular pattern with a more localised spanwise extent of about a local chord, typically referred to as shock buffet. This paper has hence presented a study contrasting this unique experimental dynamic pressure-sensitive paint dataset with scale-resolving detached-eddy simulations to help elucidate these unsteady edge-of-the-envelope flow phenomena. We focus our efforts in the vicinity where flow unsteadiness is first observed numerically which poses a challenge in simulating separating and reattaching shallow shear layers. First, we have shown that a vorticity-informed subgrid length scale yields an earlier transition from modelled to resolved turbulence, when compared to standard delayed detached-eddy simulation, and is required for more truthfully reproducing the experimental data. Second, we succeed in analysing these massive datasets with data-based modal identification techniques, actively explored in the global fluid mechanics community, enabling direct quantitative comparison with the experiment based on salient modal features.

Specifically, time-marching scale-resolving simulations have shown that at critical conditions trailing-edge and shock-induced separations merge and cells of localised separated flow repeatedly perturb the shock wave, and vice versa,

via a self-sustaining mechanism. Although, as previously demonstrated, standard delayed detached-eddy simulation improves upon unsteady Reynolds-averaged Navier–Stokes simulation well beyond shock-buffet onset conditions, the vorticity-sensitive subgrid length scale unlocks, by its construction, turbulent content earlier and better resolves the unsteadiness constituting shock buffet at onset conditions. Dominant modes from proper orthogonal decomposition and dynamic mode decomposition exhibit spatial structures with the greatest contribution on the outboard shock and its separated region downstream. Shock oscillation confined to the wing-tip region results in spanwise pressure propagation in the outboard direction. A shear-layer mode, resembling a Kelvin–Helmholtz-type instability, has been identified to co-exist with the shock-buffet phenomenon. The classical subgrid length scale based on maximum edge length predicts nearly periodic oscillations at a Strouhal number of approximately 0.22, based on mean aerodynamic chord and reference velocity. However, the second simulation incorporating the solution-dependent vorticity vector gives a more irregular signal with broadband content centred at a Strouhal number of approximately 0.27. Equivalent modes identified from dynamic pressure-sensitive paint data highlight a striking similarity dominated by outboard pressure propagation along and downstream of the shock in the same broadband frequency range that characterises swept-wing shock buffet. However, even though the vorticity-sensitive simulation results in remarkable agreement with the experimental dataset overall, the lower-frequency shock unsteadiness behaviour is unique to the wind-tunnel test and does not feature in the fully developed buffet phase of the fluid-only numerical analyses.

Possible sources for this discrepancy re low-frequency unsteadiness in the experiment are numerous: external forcing from varying freestream turbulence levels in the wind tunnel environment, the model's structural dynamics considering the inherent flexibility of large aircraft wing models, turbulent structures within the upstream boundary layer and the dynamics between the shock wave and the separated region, or an intrinsic property of the shock-wave/boundary-layer interaction. Identifying a unique source is challenging and likely requires highest-fidelity simulation featuring fluid-structure interaction in the wind-tunnel environment and a fully-resolved boundary layer.

Acknowledgements

References

[1] Hilton, W. F., and Fowler, R. G., "Photographs of Shock Wave Movement," Tech. Rep. NPL R&M No. 2692, National Physical Laboratory, 1947.

[2] McDevitt, J. B., and Okuno, A. F., "Static and Dynamic Pressure Measurements on a NACA 0012 Airfoil in the Ames High

Reynolds Number Facility," Tech. Rep. NASA TP 2485, Jun. 1985.

[3] Jacquin, L., Molton, P., Deck, S., Maury, B., and Soulevant, D., "Experimental Study of Shock Oscillation over a Transonic Supercritical Profile," *AIAA Journal*, Vol. 47, No. 9, 2009, pp. 1985–1994.

[4] Feldhusen-Hoffmann, A., Statnikov, V., Klaas, M., and Schröder, W., "Investigation of Shock–Acoustic-Wave Interaction in Transonic Flow," *Experiments in Fluids*, Vol. 59, No. 15, 2018, pp. 1–13.

[5] Brunet, V., "Computational Study of Buffet Phenomenon with Unsteady RANS Equations," 2003. AIAA Paper 2003-2679.

[6] Deck, S., "Numerical Simulation of Transonic Buffet over a Supercritical Airfoil," *AIAA Journal*, Vol. 43, No. 7, 2005, pp. 1556–1566.

[7] Xiao, Q., Tsai, H.-M., and Liu, F., "Numerical Study of Transonic Buffet on a Supercritical Airfoil," *AIAA Journal*, Vol. 44, No. 3, 2006, pp. 620–628.

[8] Iovnovich, M., and Raveh, D. E., "Reynolds-Averaged Navier-Stokes Study of the Shock-Buffet Instability Mechanism," *AIAA Journal*, Vol. 50, No. 4, 2012, pp. 880–890.

[9] Grossi, F., Braza, M., and Hoarau, Y., "Prediction of Transonic Buffet by Delayed Detached-Eddy Simulation," *AIAA Journal*, Vol. 52, No. 10, 2014, pp. 2300–2312.

[10] Lee, B. H. K., "Self-Sustained Shock Oscillations on Airfoils at Transonic Speeds," *Progress in Aerospace Sciences*, Vol. 37, No. 2, 2001, pp. 147–196.

[11] Lee, B. H. K., "Oscillatory Shock Motion Caused by Transonic Shock Boundary-Layer Interaction," *AIAA Journal*, Vol. 28, No. 5, 1990, pp. 942–944.

[12] Hartmann, A., Feldhusen, A., and Schröder, W., "On the Interaction of Shock Waves and Sound Waves in Transonic Buffet Flow," *Physics of Fluids*, Vol. 25, No. 026101, 2013, pp. 1–17.

[13] Hartmann, A., Klaas, M., and Schröder, W., "Coupled Airfoil Heave/Pitch Oscillations at Buffet Flow," *AIAA Journal*, Vol. 51, No. 7, 2013, pp. 1542–1552.

[14] Crouch, J., Garbaruk, A., Magidov, D., and Travin, A., "Origin of Transonic Buffet on Aerofoils," *Journal of Fluid Mechanics*, Vol. 628, 2009, pp. 357–369.

[15] Sartor, F., Mettot, C., and Sipp, D., "Stability, Receptivity, and Sensitivity Analyses of Buffeting Transonic Flow over a Profile," *AIAA Journal*, Vol. 53, No. 7, 2014, pp. 1980–1993.

[16] Garnier, E., and Deck, S., "Large-Eddy Simulation of Transonic Buffet over a Supercritical Airfoil," *Turbulence and Interactions: Proceedings the TI 2009 Conference*, edited by M. Deville, T.-H. Lê, and P. Sagaut, Springer Berlin Heidelberg, Berlin, Heidelberg, 2010, pp. 135–141.

[17] Fukushima, Y., and Kawai, S., "Wall-modeled Large-Eddy Simulation of Transonic Buffet over a Supercritical Airfoil at high Reynolds Number," 2017. AIAA Paper 2017-0495.

[18] Brion, V., Dandois, J., Abart, J.-C., and Paillart, P., "Experimental Analysis of the Shock Dynamics on a Transonic Laminar Airfoil," *Progress in Flight Physics*, Vol. 9, 2017, pp. 365–386.

[19] Dandois, J., Mary, I., and Brion, V., "Large-Eddy Simulation of Laminar Transonic Buffet," *Journal of Fluid Mechanics*, Vol. 850, 2018, pp. 156–178.

[20] Zauner, M., De Tullio, N., and Sandham, N. D., "Direct Numerical Simulations of Transonic Flow Around an Airfoil at Moderate Reynolds Numbers," *AIAA Journal*, Vol. 57, No. 2, 2019, pp. 597–607.

[21] Giannelis, N., Vio, G., and Levinski, O., "A Review of Recent Developments in the Understanding of Transonic Shock Buffet," *Progress in Aerospace Sciences*, Vol. 92, 2017, pp. 39–84.

[22] Hwang, C., and Pi, W. S., "Northrop F-5 A Aircraft Transonic Buffet Pressure Data Acquisition and Response Analysis," *Journal of Aircraft*, Vol. 12, No. 9, 1975, pp. 714–720.

[23] Riddle, D., "Wind-Tunnel Investigation of Surface-Pressure Fluctuations Associated with Aircraft Buffet," 1975. AIAA Paper 1975-0067.

[24] Roos, F., "The Buffeting Pressure Field of a High-Aspect-Ratio Swept Wing," 1985. AIAA Paper 1985-1609.

[25] Benoit, B., and Legrain, I., "Buffeting Prediction for Transport Aircraft Applications Based on Unsteady Pressure Measurements," 1987. AIAA Paper 1987-2356.

[26] Dandois, J., "Experimental Study of Transonic Buffet Phenomenon on a 3D Swept Wing," *Physics of Fluids*, Vol. 28, No. 016101, 2016, pp. 1–17.

[27] Koike, S., Ueno, M., Nakakita, K., and Hashimoto, A., "Unsteady Pressure Measurement of Transonic Buffet on NASA Common Research Model," 2016. AIAA Paper 2016-4044.

[28] Lawson, S., Greenwell, D., and Quinn, M. K., "Characterisation of Buffet on a Civil Aircraft Wing," 2016. AIAA Paper 2016-1309.

[29] Steimle, P. C., Karhoff, D.-C., and Schröder, W., "Unsteady Transonic Flow over a Transport-Type Swept Wing," *AIAA Journal*, Vol. 50, No. 2, 2012, pp. 399–415.

[30] Merienne, M.-C., Le Sant, Y., Lebrun, F., Deleglise, B., and Sonnet, D., "Transonic Buffeting Investigation Using Unsteady Pressure-Sensitive Paint in a Large Wind Tunnel," 2013. AIAA Paper 2013-1136.

[31] Sugioka, Y., Koike, S., Nakakita, K., Numata, D., Nonomura, T., and Asai, K., "Experimental Analysis of Transonic Buffet on a 3D Swept Wing Using Fast-Response Pressure-Sensitive Paint," *Experiments in Fluids*, Vol. 59, No. 108, 2018, pp. 1–20.

[32] Iovnovich, M., and Raveh, D. E., "Numerical Study of Shock Buffet on Three-Dimensional Wings," *AIAA Journal*, Vol. 53, No. 2, 2015, pp. 449–463.

[33] Plante, F., Dandois, J., and Laurendeau, É., "Similarities Between Cellular Patterns Occurring in Transonic Buffet and Subsonic Stall," *AIAA Journal*, , No. 58, ???? doi:10.2514/1.J058555.

[34] Crouch, J. D., Garbaruk, A., and Strelets, M., "Global instability in the onset of transonic-wing buffet," *Journal of Fluid Mechanics*, Vol. 881, 2019, pp. 3–22. doi:10.1017/jfm.2019.748.

[35] Plante, F., Dandois, J., Beneddine, S., Sipp, D., and Laurendeau, E., "Numerical simulations and global stability analyses of transonic buffet and subsonic stall," *54th 3AF International Conference on Applied Aerodynamics*, 2019. FP63-AERO2019-plante.

[36] Paladini, E., Beneddine, S., Dandois, J., Sipp, D., and Robinet, J.-C., "Transonic buffet instability: From two-dimensional airfoils to three-dimensional swept wings," *Phys. Rev. Fluids*, Vol. 4, 2019, p. 103906. doi:10.1103/PhysRevFluids.4.103906.

[37] Brunet, V., and Deck, S., "Zonal-Detached Eddy Simulation of Transonic Buffet on a Civil Aircraft Type Configuration," 2008. AIAA Paper 2008-4152.

[38] Ishida, T., Hashimoto, A., Ohmichi, Y., Aoyama, T., and Takekawa, K., "Transonic Buffet Simulation over NASA-CRM by Unsteady-FaSTAR Code," 2017. AIAA Paper 2017-0494.

[39] Sartor, F., and Timme, S., "Delayed Detached-Eddy Simulation of Shock Buffet on Half Wing-Body Configuration," *AIAA Journal*, Vol. 55, No. 4, 2017, pp. 1230–1240.

[40] Timme, S., "Global Instability of Wing Shock-Buffet Onset," *Journal of Fluid Mechanics*, Vol. 885, 2020, p. A37. doi: 10.1017/jfm.2019.1001.

[41] Masini, L., Timme, S., Ciarella, A., and Peace, A. J., "Influence of Vane Vortex Generators on Transonic Wing Buffet: Further Analysis of the BUCOLIC Experimental Dataset," *52nd 3AF International Conference on Applied Aerodynamics*, 2017. FP14-AERO2017-masini.

[42] Masini, L., Timme, S., and Peace, A. J., "Analysis of a Civil Aircraft Wing Transonic Shock Buffet Experiment," *Journal of Fluid Mechanics*, Vol. 884, No. A1, 2020, pp. 1–42.

[43] Sartor, F., and Timme, S., "Reynolds-Averaged Navier-Stokes Simulations of Shock Buffet on Half Wing-Body Configuration," 2015. AIAA Paper 2015-1939.

[44] Shur, M. L., Spalart, P. R., Strelets, M., and Travin, A. K., "An enhanced version of DES with rapid transition from RANS to LES in separated flows," *Flow, Turbulence and Combustion*, Vol. 95, No. 4, 2015, pp. 709–737.

[45] Taira, K., Brunton, S. L., Dawson, S. T. M., Rowley, C. W., Colonius, T., McKeon, B. J., Schmidt, O. T., Stanislav, S., Theofilis, V., and Ukeiley, L. S., "Modal Analysis of Fluid Flows: An Overview," *AIAA Journal*, Vol. 55, No. 12, 2017, pp. 4013–4041.

[46] Ohmichi, Y., Ishida, T., and Hashimoto, A., "Modal Decomposition Analysis of Three-Dimensional Transonic Buffet Phenomenon on a Swept Wing," *AIAA Journal*, Vol. 56, No. 10, 2018, pp. 3938–3950.

[47] Timme, S., and Thormann, R., "Towards Three-Dimensional Global Stability Analysis of Transonic Shock Buffet," 2016. AIAA Paper 2016-3848.

[48] Shaw, J. A., Stokes, S., and Lucking, M. A., "The Rapid and Robust Generation of Efficient Hybrid Grids for RANS Simulations over Complete Aircraft," *International Journal for Numerical Methods in Fluids*, Vol. 43, No. 6-7, 2003, pp. 785–821.

[49] Rudnik, R., Melber-Wilkending, S., and Risley-Settle, P., "TAU-SOLAR Contributions to the 3rd High Lift Prediction Workshop," 2018. AIAA Paper 2018-1035.

[50] Allmaras, S. R., Johnson, F. T., and Spalart, P. R., "Modifications and Clarifications of the Spalart-Allmaras Turbulence Model," 2012. ICCFD7-1902.

[51] Probst, A., and Reuß, S., "Scale-Resolving Simulations of Wall-Bounded Flows with an Unstructured Compressible Flow Solver," *Progress in Hybrid RANS-LES Modelling*, Vol. 130, 2015, pp. 481–491.

[52] Probst, A., and Reuß, S., "Progress in Scale-Resolving Simulations with the DLR-TAU Code," Tech. Rep. 420051, DLR, 2016.

[53] Löwe, J., Probst, A., Knopp, R., and Jarrin, N., "A Low-Dissipation Low-Dispersion Second-Order Scheme for Unstructured Finite-Volume Flow Solvers," 2015. AIAA Paper 2015-0815.

[54] Probst, A., Löwe, J., Reuß, S., and Kessler, R., "Scale-Resolving Simulations with a Low-Dissipation Low-Dispersion Second-Order Scheme for Unstructured Finite-Volume Flow Solvers," 2015. AIAA Paper 2015-0816.

[55] Spalart, P., *Trends in turbulence treatments*, 2000. doi:10.2514/6.2000-2306.

[56] Crouch, J., Garbaruk, A., and Magidov, D., "Predicting the Onset of Flow Unsteadiness Based on Global Instability," *Journal of Computational Physics*, Vol. 224, No. 2, 2007, pp. 924–940.

[57] Plante, F., and Laurendeau, E., "Simulation of Transonic Buffet Using a Time-Spectral Method," *AIAA Journal*, Vol. 57, 2019, pp. 1–13. doi:10.2514/1.j057224.

[58] Spalart, P. R., Strelets, W.-H., and Allmaras, S. R., "Comments on the feasibility of LES for wings, and on a hybrid RANS/LES approach," *Proceedings of first AFOSR international conference on DNS/LES*, 1997.

[59] Travin, A., Shur, M., Strelets, M., and Spalart, P. R., "Detached-eddy simulations past a circular cylinder," *Flow, Turbulence and Combustion*, Vol. 63, No. 1, 2000, pp. 293–313.

[60] Spalart, P. R., Deck, S., Shur, M. L., Squires, K. D., Strelets, M. K., and Travin, A., "A New Version of Detached-Eddy Simulation, Resistant to Ambiguous Grid Densities," *Theoretical and Computational Fluid Dynamics*, Vol. 20, No. 3, 2006, pp. 181–195.

[61] Spalart, P. R., "Detached-eddy Simulation," *Annual Review of Fluid Mechanics*, Vol. 41, 2009, pp. 181–202.

[62] Breuer, M., "Large eddy simulation of the subcritical flow past a circular cylinder: Numerical and modeling aspects," *International Journal for Numerical Methods in Fluids*, Vol. 28, No. 9, 1998, pp. 1281–1302.

[63] Mockett, C., Fuchs, M., Garbaruk, A., Shur, M., Spalart, P., Strelets, M., Thiele, F., and Travin, A., "Two Non-Zonal Approaches to Accelerate RANS to LES Transition of Free Shear Layers in DES," *Progress in Hybrid RANS-LES Modelling*, Vol. 130, edited by S. Girimaji, W. Haase, S.-H. Peng, and D. Schwamborn, Springer International Publishing, 2015, pp. 187–201.

[64] Chauvet, N., Deck, S., and Jacquin, L., "Zonal Detached Eddy Simulation of a Controlled Propulsive Jet," *AIAA Journal*, Vol. 45, No. 10, 2007, pp. 2458–2473.

[65] Spalart, P. R., "Young-Person's Guide to Detached-Eddy Simulation Grids," Tech. Rep. CR-2001-211032, NASA, 2001.

[66] Sirovich, L., "Turbulence and the Dynamics of Coherent Structures. I. Coherent Structures," *Quarterly of Applied Mathematics*, Vol. 45, No. 3, 1987, pp. 561–571.

[67] Belson, B. A., Tu, J. H., and Rowley, C. W., "Algorithm 945: Modred—a Parallelized Model Reduction Library," *ACM Transactions on Mathematical Software*, Vol. 40, No. 4, 2014, pp. 1–23.

[68] Sartor, F., and Timme, S., "Mach Number Effects on Buffeting Flow on a Half Wing-Body Configuration," *International Journal of Heat and Fluid Flow*, Vol. 26, No. 7, 2016, pp. 2066–2080.

[69] Burg, J. P., "Maximum Entropy Spectral Analysis," *37th Annual International Meeting of the Society of Exploration Geophysicists*, 1967.

[70] Welch, P., "The Use of Fast Fourier Transform for the Estimation of Power Spectra: A Method Based on Time Averaging over Short, Modified Periodograms," *IEEE Transaction on Audio and Electroacoustics*, Vol. 15, No. 2, 1967, pp. 70–73.

[71] Tu, J. H., Rowley, C. W., Luchtenburg, D. M., Brunton, S. L., and Kutz, J. N., "On Dynamic Mode Decomposition: Theory and Applications," *Journal of Computational Dynamics*, Vol. 1, No. 2, 2014, pp. 391–421.